Planet migration in massive circumbinary disks

Matthew Teasdale

A thesis submitted in partial fulfilment
of the requirements for the degree of
Master of Science

Jeremiah Horrocks Institute for Mathematics, Physics and Astronomy
University of Central Lancashire

December 2022

Declaration

Type of Award: Master of Science

School: Natural Sciences

I declare that while registered as a candidate for the research degree, I have not been a registered candidate or enrolled student for another award of the University or other academic or professional institution.

I declare that no material contained in the thesis has been used in any other submission for an academic award and is solely my own work.

No proof-reading service was used in the compilation of this thesis.

Matthew Teasdale

December 2022

Abstract

Most stars exist in multi-star systems, with the majority of those being binaries. Protoplanetary disks are common among young stars and are known to affect the formation and evolution of planets. To date almost 370 planets have been confirmed in binary star systems and therefore the evolution of these planets is an important area of research. We investigate the migration of gas giant planets embedded in circumbinary disks using the three-dimensional smooth particle hydrodynamic code SEREN. Firstly, a planet embedded in the massive disk of a single star system is simulated using parameters from Stamatellos & Inutsuka (2018) before planets in massive circumbinary disks are simulated. The binary parameters are varied to see their effect on the migration of the gas giant planet. We find that a planet in a massive circumbinary disk consistently undergoes a period of rapid inward migration before undergoing a slow outward migration, i.e. a Type I migration followed by a non-standard Type II migration. We find that the initial binary mass ratio has little effect on the migration timescale of the planet. We also find that a larger initial binary separation leads to higher final semi-major axis for the planet. Finally, we find that increasing the initial binary eccentricity leads to a faster outward migration of the planet, in several cases reaching beyond the initial semi-major axis in a relatively short timescale. Therefore, we find that the initial binary eccentricity has the greatest effect on the orbital migration of the planet in a massive circumbinary disk.

Contents

Declaration ii

Abstract iii

Acknowledgements xiii

1 Introduction 1

1.1 Exoplanets 1

1.2 Binary stars with planetary systems 2

1.3 Protoplanetary disks 3

1.4 Gas giant planet formation 4

1.4.1 Core accretion 4

1.4.2 Gravitational instability 5

1.5 Planetary migration 6

1.5.1 Type I migration 7

1.5.2 Type II migration 7

1.6 Migration Timescale 7

1.7 Thesis outline 9

2 Computational Methods 10

2.1 Smooth Particle Hydrodynamics 10

2.2 Initial Conditions 12

2.2.1 Disk surface density profile 12
2.2.2 Disk temperature 12
2.2.3 Disk thickness 13
2.2.4 Disk rotation 13
2.3 Sinks 14
2.4 Disk thermodynamics 14
2.4.1 Initial conditions of the binary systems 15

3 Planetary migration in a disk around a single solar mass star 16
3.1 Initial conditions of the benchmark run 16
3.1.1 Convergence 16
3.1.2 Settling the disk 19
3.2 Benchmark run 21

4 Planetary migration in a disk around a binary system 27
4.1 Run 1: 0.5 - 0.5 $M_\odot$, $\alpha_b = 1$ AU, $e_b = 0$ 29
4.2 Run 2: 0.5 - 0.5 $M_\odot$, $\alpha_b = 1$ AU, $e_b = 0.2$ 30
4.3 Run 3: 0.5 - 0.5 $M_\odot$, $\alpha_b = 5$ AU, $e_b = 0$ 33
4.4 Run 4: 0.5 - 0.5 $M_\odot$, $\alpha_b = 5$ AU, $e_b = 0.2$ 34
4.5 Run 5: 0.5 - 0.5 $M_\odot$, $\alpha_b = 5$ AU, $e_b = 0.5$ 35
4.6 Run 6: 0.8 - 0.2 $M_\odot$, $\alpha_b = 1$ AU, $e_b = 0$ 38
4.7 Run 7: 0.8 - 0.2 $M_\odot$, $\alpha_b = 1$ AU, $e_b = 0.2$ 39
4.8 Run 8: 0.8 - 0.2 $M_\odot$, $\alpha_b = 5$ AU, $e_b = 0$ 41
4.9 Run 9: 0.8 - 0.2 $M_\odot$, $\alpha_b = 5$ AU, $e_b = 0.2$ 42
4.10 Run 10: 0.8 - 0.2 $M_\odot$, $\alpha_b = 5$ AU, $e_b = 0.5$ 43

5 Discussion 45
5.1 Role of the initial binary mass ratio on the migration of the planet . . 45
5.2 Role of the initial binary separation on the migration of the planet . . 46

5.3 Role of the initial binary eccentricity on the migration of the planet . 47
5.4 Caveats 50
5.5 Summary and conclusion 51

List of Tables

3.1 Semi-major axis α, migration timescale $\tau_{\rm mig}$, planet mass $M_{\rm P}$ and migration velocity $v_{\rm mig}$ for the benchmark run. Here, the negative values indicate the planet is migrating in an outward direction. 23

4.1 The ten simulations run for this project, with the binary parameters listed. 28

4.2 The semi-major axis α, migration timescale $\tau_{\rm mig}$, mass $M_{\rm P}$ and migration velocity $v_{\rm mig}$ of the planet at different times, for Run 1. The binary consists of two $0.5\,{\rm M}_{\odot}$ stars, and initially has zero eccentricity $e_{\rm b}=0$ and semi-major axis $\alpha_{\rm b}=1\,{\rm AU}$. Here, the negative values in $v_{\rm mig}$ indicate the planet is migrating in an outward direction. 30

4.3 The semi-major axis α, migration timescale $\tau_{\rm mig}$, mass $M_{\rm P}$ and migration velocity $v_{\rm mig}$ of the planet at different times, for Run 2. The binary consists of two $0.5\,{\rm M}_{\odot}$ stars, and initially has eccentricity $e_{\rm b}=0.2$ and semi-major axis $\alpha_{\rm b}=1\,{\rm AU}$. Here, the negative values in $\tau_{\rm mig}$ and in $\rm v_{mig}$ indicate the planet is migrating in an outward direction. . . . 31

4.4 The semi-major axis α, migration timescale $\tau_{\rm mig}$, mass $M_{\rm P}$ and migration velocity $v_{\rm mig}$ of the planet at different times, for Run 3. The binary consists of two $0.5\,{\rm M}_{\odot}$ stars, and initially has eccentricity $e_{\rm b}=0$ and semi-major axis $\alpha_{\rm b}=5\,{\rm AU}$. Here, the negative values in $v_{\rm mig}$ indicate the planet is migrating in an outward direction. 34

4.5 The semi-major axis α, migration timescale $\tau_{\rm mig}$, mass $M_{\rm P}$ and migration velocity $v_{\rm mig}$ of the planet at different times, for Run 4. The binary consists of two $0.5\,{\rm M}_{\odot}$ stars, and initially has eccentricity $e_{\rm b}=0.2$ and semi-major axis $\alpha_{\rm b}$ =5 AU. Here, the negative values in $v_{\rm mig}$ indicate the planet is migrating in an outward direction. 35

4.6 The semi-major axis α, migration timescale $\tau_{\rm mig}$, mass $M_{\rm P}$ and migration velocity $v_{\rm mig}$ of the planet at different times, for Run 5. The binary consists of two $0.5\,{\rm M}_{\odot}$ stars, and initially has eccentricity $e_{\rm b}=0.5$ and semi-major axis $\alpha_{\rm b}$ =5 AU. Here, the negative values in $v_{\rm mig}$ indicate the planet is migrating in an outward direction. 36

4.7 The semi-major axis α, migration timescale $\tau_{\rm mig}$, mass $M_{\rm P}$ and migration velocity $v_{\rm mig}$ of the planet at different times, for Run 6. This system consists of a $0.8\,{\rm M}_{\odot}$ star and a $0.2\,{\rm M}_{\odot}$ star, and initially has eccentricity $e_{\rm b}=0$ and semi-major axis $\alpha_{\rm b}$ =1 AU. Here, the negative values in $v_{\rm mig}$ indicate the planet is migrating in an outward direction. 38

4.8 The semi-major axis α, migration timescale $\tau_{\rm mig}$, mass $M_{\rm P}$ and migration velocity $v_{\rm mig}$ of the planet at different times, for Run 7. This system consists of a $0.8\,{\rm M}_{\odot}$ star and a $0.2\,{\rm M}_{\odot}$ star, and initially has eccentricity $e_{\rm b}=0.2$ and semi-major axis $\alpha_{\rm b}=1$ AU. Here, the negative values in $v_{\rm mig}$ indicate the planet is migrating in an outward direction. 39

4.9 The semi-major axis α, migration timescale $\tau_{\rm mig}$, mass $M_{\rm P}$ and migration velocity $v_{\rm mig}$ of the planet at different times, for Run 8. This system consists of a $0.8\,{\rm M}_{\odot}$ star and a $0.2\,{\rm M}_{\odot}$ star, and initially has eccentricity $e_{\rm b}=0$ and semi-major axis $\alpha_{\rm b}$ =5 AU. Here, the negative values in $v_{\rm mig}$ indicate the planet is migrating in an outward direction. 41

4.10 The semi-major axis α, migration timescale $\tau_{\rm mig}$, mass $M_{\rm P}$ and migration velocity $v_{\rm mig}$ of the planet at different times, for Run 9. This system consists of a $0.8\,{\rm M}_{\odot}$ star and a $0.2\,{\rm M}_{\odot}$ star, and initially has eccentricity $e_{\rm b}=0.2$ and semi-major axis $\alpha_{\rm b}=5\,{\rm AU}$. Here, the negative values in $v_{\rm mig}$ indicate the planet is migrating in an outward direction. 42

4.11 The semi-major axis α, migration timescale $\tau_{\rm mig}$, mass $M_{\rm P}$ and migration velocity $v_{\rm mig}$ of the planet at different times, for Run 10. This system consists of a $0.8\,{\rm M}_{\odot}$ star and a $0.2\,{\rm M}_{\odot}$ star, and initially has eccentricity $e_{\rm b}=0.5$ and semi-major axis $\alpha_{\rm b}=5\,{\rm AU}$. Here, the negative values in $v_{\rm mig}$ indicate the planet is migrating in an outward direction. 43

List of Figures

1.1 The masses of all currently confirmed exoplanets plotted against their semi-major axis. Courtesy NASA/JPL-Caltech. 2

3.1 A comparison of 0.5×10^5, 1×10^5, 2×10^5, 2.5×10^5, 3×10^5, 4×10^5, 5×10^5, 6×10^5 and 10×10^5 SPH particle simulations. The 10×10^5 SPH particle simulation is data taken from Stamatellos & Inutsuka (2018). This plot shows the evolution of the planet's (a) semi-major axis (b) mass and (c) eccentricity over a period of 20 kyr (top to bottom). 18

3.2 A comparison of simulations with disks relaxed for 2 kyr, 3 kyr and 5 kyr. Here the (a) semi-major axis (b) mass and (c) eccentricity of the planet are shown as it evolves for 20 kyr. 20

3.3 The evolution of the surface density of the disk for the benchmark run: $1\,M_J$ planet embedded in a $0.1\,M_\odot$ disk (represented by 5×10^5 SPH particles) around a $1\,M_\odot$ star as it evolves for 20 kyr. 24

3.4 The evolution of the (a) semi-major axis (b) mass and (c) eccentricity of a $1\,M_J$ planet embedded in a 5×10^5 SPH particle disk orbiting a $1\,M_\odot$ star (the benchmark run). We also compare this run with that from Stamatellos & Inutsuka (2018). 25

3.5 The initial surface density(top), the temperature profile (middle), and Toomre parameter (bottom) of the disk for the benchmark run. . . . 26

4.1 $1\,M_J$ planet embedded in a disk orbiting a binary system consisting of two $0.5\,M_\odot$ stars, with initial semi-major axis $\alpha_b = 1\,AU$ and eccentricity $e_b = 0$ and $e_b = 0.2$. (a) The evolution of the semi-major axis of the planet, (b) the evolution of the planet's mass, and (c) the evolution of the planet's eccentricity. The disk modelled here has been settled for 3 kyr. 32

4.2 $1\,M_J$ planet embedded in a disk orbiting a binary system consisting of two $0.5\,M_\odot$ stars, with initial semi-major axis $\alpha_b = 5\,AU$ and eccentricity $e_b = 0$, $e_b = 0.2$ and $e_b = 0.5$. (a) The evolution of the semi-major axis of the planet, (b) the evolution of the planet's mass, and (c) the evolution of the planet's eccentricity. The disk modelled here has been settled for 3 kyr. 37

4.3 $1\,M_J$ planet embedded in a disk orbiting a binary system consisting of a $0.8\,M_\odot$ star and a $0.2\,M_\odot$ star, with initial semi-major axis $\alpha_b = 1\,AU$ and eccentricity $e_b = 0$ and $e_b = 0.2$. (a) The evolution of the semi-major axis of the planet, (b) the evolution of the planet's mass, and (c) the evolution of the planet's eccentricity. The disk modelled here has been settled for 3 kyr. 40

4.4 $1\,M_J$ planet embedded in a disk orbiting a binary system consisting of a $0.8\,M_\odot$ star and a $0.2\,M_\odot$ star, with initial semi-major axis $\alpha_b = 5\,AU$ and eccentricity $e_b = 0$, $e_b = 0.2$ and $e_b = 0.5$. (a) The evolution of the semi-major axis of the planet, and (b) the evolution of the planet's mass. The disk modelled here has been settled for 3 kyr. 44

5.1 $1\,M_J$ planet embedded in a disk orbiting a binary system consisting of two $0.5\,M_\odot$ stars, with initial semi-major axis $\alpha_b = 1\,AU$ and $\alpha_b = 5\,AU$ and eccentricity $e_b = 0$, $e_b = 0.2$ and $e_b = 0.5$ (as marked on the graph). (a) The evolution of the semi-major axis of the planet, (b) the evolution of the planet's mass, and (c) the evolution of the planet's eccentricity. The disk modelled here has been settled for 3 kyr. 48

5.2 $1\,M_J$ planet embedded in a disk orbiting a binary system consisting of a $0.8\,M_\odot$ star and a $0.2\,M_\odot$ star, with initial semi-major axis $\alpha_b = 1\,AU$ and $\alpha_b = 5\,AU$ and eccentricity $e_b = 0$, $e_b = 0.2$ and $e_b = 0.5$. (a) The evolution of the semi-major axis of the planet, (b) the evolution of the planet's mass, and (c) the evolution of the planet's eccentricity. The disk modelled here has been settled for 3 kyr. 49

5.3 The evolution of the semi-major axis of the planet (top left), its mass (top right), its migration timescale (bottom left) and its migration velocity (bottom right) at different times for all simulations presented in this thesis. The two colours correspond to different stellar mass ratios: magenta indicates a $0.5\,M_\odot$ - $0.5\,M_\odot$ binary and cyan, a $0.8\,M_\odot$ - $0.2\,M_\odot$ binary. The three symbols indicate the initial eccentricity of the binary, with a diamond corresponding to $e_b = 0$, a triangle to $e_b = 0.2$ and a pentagon to $e_b = 0.5$. Finally filled symbols correspond to an initial binary separation of $\alpha_b = 1\,AU$ and unfilled symbols an initial separation of $\alpha_b = 5\,AU$. 53

Acknowledgements

I would like to thank my supervisory team, Dr Dimitris Stamatellos, Dr Daniel Holdsworth and Professor Silvia Dalla for their help and suggestions when constructing this thesis. I would also like to thank Adam Fenton and Ethan Carter for their help and suggestions with the various coding aspects of this project. The simulations produced would not have been possible without the use of UCLan's high performance computing facility. Finally I would like to thank my friends and family for their support throughout this project.

Chapter 1

Introduction

1.1 Exoplanets

Since the discovery of the first exoplanet, orbiting the pulsar PSR 1257+12 (Wolszczan & Frail, 1992), the research into the dynamics of planets has grown considerably with all currently confirmed exoplanets seen in Fig 1.1. This research is typically divided into two distinct groups, observation based and simulation based with comparisons being made between them (Hallam & Paardekooper, 2020). As of publication, over 5000 exoplanets have been confirmed[1].

As defined by the IAU, a planet is an object that orbits around a star, it has sufficient mass to attain hydrostatic equilibrium and therefore a nearly spherical shape, and has cleared the neighbourhood around its orbit (Binzel, 2006). In addition to these, the object's mass must be below $13\,M_J$ as to not sustain deuterium burning in its interior. If its mass is above this value then it is considered a brown dwarf (Spiegel, Burrows & Milsom, 2011).

Exoplanets are grouped into different populations according to their mass and orbital radius. For giant planets of equal mass or larger than Saturn, and orbits from a few tenths of an AU out to the orbital radius of Jupiter, they are classified

[1]NASA Exoplanet Archive, DOI: 10.26133/NEA12 (Accessed on: 06/09/2022).

as warm and cold Jupiters (Armitage, 2020). Hot Jupiters are giant planets that orbit closer in, at around $\alpha = 0.1\,\mathrm{AU}$, and have high effective temperatures. Giant planets with an orbital radius about $\alpha \gtrsim 8\,\mathrm{AU}$ are classified as wide-orbit giant planets and are typically twice the mass of Jupiter (Wagner, Apai & Kratter, 2019). The question as to their origin is still outstanding and it is open whether they form entirely different to closer in giant planets.

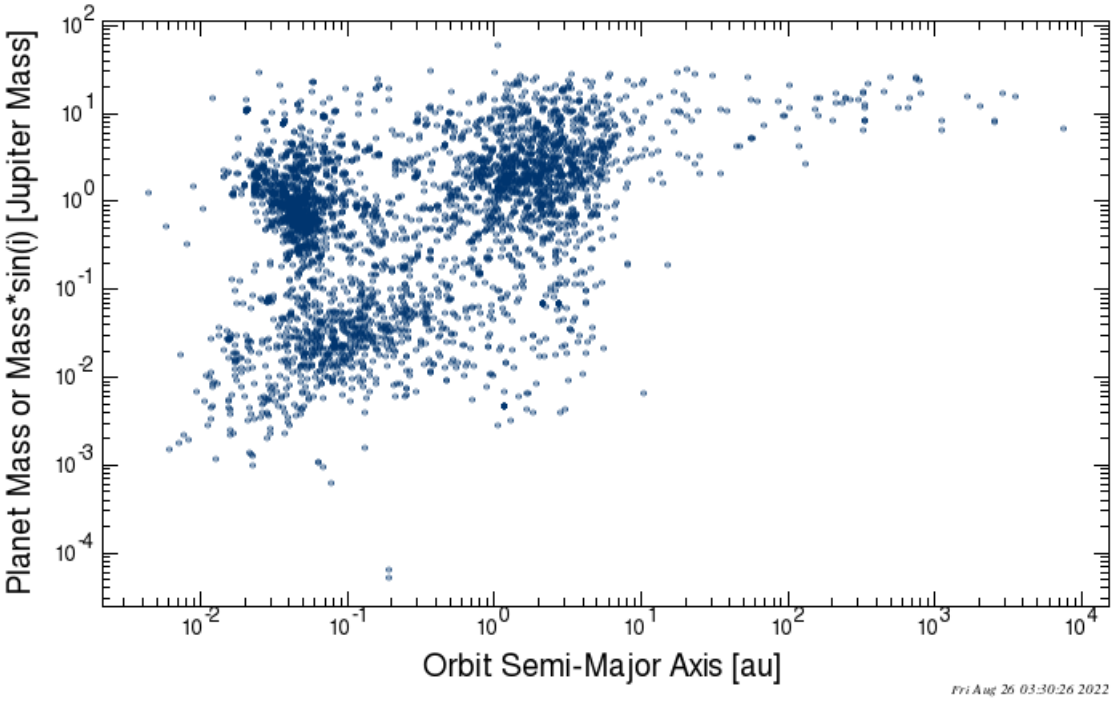

Figure 1.1: The masses of all currently confirmed exoplanets plotted against their semi-major axis. Courtesy NASA/JPL-Caltech.

1.2 Binary stars with planetary systems

Just under half of star systems observed exist within multi-star systems. Raghavan et al. (2010) studied a sample of 454 stars selected from the Hipparcos catalog within the solar neighbourhood. This study found that 44% stars exist within multi-star

systems with 150 of the sample stars being in binary systems.

Planets orbiting binaries are observed to come in three distinct types; S or satellite type, P or primary type and L or librator type (Dvorak, Froeschle & Froeschle, 1986). P-type, or circumbinary, describes a system in which the planet orbits the two stars together. The first circumbinary planet detected was Kepler-16b (Doyle et al., 2011) and since then 28 have been confirmed as P-type (Su et al., 2021). S-type, or circumstellar, describes a system in which a planet orbits one of the stars of the binary. Currently over 211 S-type planets have been confirmed, which account for the majority of planets discovered in binary systems (Su et al., 2021). Finally L-type describes a planet librating around the Lagrangian L_4 or L_5 equilibrium points.

1.3 Protoplanetary disks

Protoplanetary disks are mostly made of gas and can be described by the equations of fluid dynamics, the conservation of energy, mass and momentum (Paardekooper et al., 2022). Goldreich & Tremaine (1980) first discussed the theory of planet-disk interaction, with the field growing significantly in the last four decades. Disks around Young Stellar Objects (YSOs) have a lifetime of a few Myr, with the majority of this time spent in the Class II phase. Class II YSOs are young pre-main sequence stars with disks around them (T Tauri stars). The vertical density profile of disks can be determined by considering the hydrostatic equilibrium in the direction perpendicular to the disk midplane, with the simplest models showing a Gaussian density profile. The temperature profile is determined by stellar irradiation, viscous dissipation within the disk, and the disk cooling. This leads to a scaling of the temperature with radius r of between $r^{-\frac{3}{4}}$ and $r^{-\frac{1}{2}}$. The evolution of the disk is expected to take place as a result of the following: (i) the redistribution of the angular momentum of the disk, moderated by the disk viscosity, (ii) the loss of mass of the disk due to accretion onto the star and planet, and (iii) the loss of angular momentum and

mass due to the presence of magnetohydrodynamic (MHD) winds (Armitage, 2015). Protoplanetary disks have been observed to be circumstellar or circumbinary with planet formation happening within these disks (Lines et al., 2016; Andrews et al., 2018; Keppler et al., 2018; Pinte et al., 2018; Teague, Bae & Bergin, 2019).

The lifetime of a disk can be inferred by observing the fall in disk fraction in different age clusters. This disk fraction implies a lifetime of 3 - 5 Myr (Armitage, 2020). However, this estimated disk lifetime does not agree with the formation timescale of Jupiters by core accretion, though it is possible these planets form through disk instability as this timescale is a few kyr instead of Myr.

1.4 Gas giant planet formation

Currently there are two widely accepted theories that have been proposed to account for the formation of gas giant planets, core accretion (CA) and gravitational instability (GI).

1.4.1 Core accretion

The core accretion model is thought to account for the origin of the majority of exoplanets currently known. This gas giant planet formation theory suggests that a core forms through the accretion of both pebbles and planetesimals within a gaseous disk. This accretion of material leads to the core having a sufficient mass to attain a gaseous envelope which continues to grow at a gradual rate. At this time the mass of the core is much more massive than the envelope. Once a critical mass is reached, a runaway accretion occurs in which the gaseous envelope is accreted. The timescale over which the gaseous envelope is accreted is 10^5 yr and the critical mass is thought to be $M_{\rm crit} = 5 - 20\,\mathrm{M}_\oplus$ (Armitage, 2020). Ikoma, Nakazawa & Emori (2000) gives

the critical mass as

$$\frac{\mathrm{M_{crit}}}{\mathrm{M_\oplus}} \approx 12 \left(\frac{\dot{\mathrm{M}}_{\mathrm{core}}}{10^{-6}\,\mathrm{M_\oplus yr^{-1}}} \right)^{\frac{1}{4}} \left(\frac{\kappa_{\mathrm{R}}}{1\,\mathrm{cm^2 g^{-1}}} \right)^{\frac{1}{4}}, \tag{1.1}$$

where κ_{R} is the Rosseland mean opacity and is assumed to be constant. This process of accretion then ceases once the planet either forms a gap in the disk or the disk itself dissipates.

The formation of giant planets via CA requires a long timescale due to the time required for the core to grow above the critical mass (Bodenheimer & Pollack, 1986). The growth of the massive core is at odds with the dispersal of the protoplanetary disk (3 - 5 Myr) and so CA is expected to produce a much higher fraction of lower mass planets compared to gas giants and brown dwarfs (Wagner, Apai & Kratter, 2019).

1.4.2 Gravitational instability

If a disk is sufficiently cold and/or massive, then the disk will be gravitationally unstable when the Toomre criterion is satisfied (Toomre, 1964),

$$Q \equiv \frac{c_{\mathrm{s}}\Omega}{\pi G \Sigma} \lesssim Q_{\mathrm{crit}} \simeq 1, \tag{1.2}$$

where Q is the Toomre parameter, G is the gravitational constant, $\mathrm{c_s}$ is the sound speed, Ω the angular frequency, and Σ the surface density of the disk. It is necessary that a massive disk be present for an instability

$$\frac{M_{\mathrm{disk}}}{M_*} \gtrsim \frac{h}{r}, \tag{1.3}$$

where M_{disk} is the mass of the disk, M_* the mass of the central star, h the scale height of the disk and r the radius of the disk. If the central star is assumed to be of solar mass and $\frac{h}{r} = 0.05$, the disk mass must be at least 10% of the stellar mass for the instability to develop. One of the outcomes of gravitational instability is fragmentation which can lead to the formation of giant planets.

Gammie (2001) shows that if the cooling time of the disk is sufficiently short, ($\Omega\,\tau_{\rm c} \lesssim 3$), then the disk can fragment. At large radii the cooling time is short therefore, fragmentation and planet formation is likely.

It has been suggested that GI commonly produces massive companions at large separations (Matzner & Levin, 2005; Clarke & Lodato, 2009; Kratter, Murray-Clay & Youdin, 2010). Therefore, many of the companions originating from GI could be brown dwarfs or low-mass stars. This is inevitable as this process begins very early while enough mass still exists within the protoplanetary disk to trigger the instability. The companions formed therefore grow rapidly in mass through accretion from the disk (Kratter, Murray-Clay & Youdin, 2010; Forgan et al., 2018).

1.5 Planetary migration

In the core accretion model (discussed in Section 1.4), Jupiters are expected to form outside the snowline ($\sim 3\,$AU for solar type stars). In this region dust particles have an ice coating which promotes fast dust growth. The coagulation of dust particles can happen fast and a core with enough mass can form so that it can accrete a gaseous envelope. As distance increases from the central star, the timescale required to form the core of wide orbit giant planets is too long due to the limited amount of dust present. Closer in, specifically within the snow line, dust particles cannot coagulate as efficiently and therefore only terrestrial planets form (their mass does not get high enough to accrete a gaseous envelope before the disk dissipates). Even closer to the star ($< 0.1\,$AU), where hot Jupiters are located, the temperature is too high ($> 1000\,$K) and dust evaporates, therefore the planet cannot form in-situ (Armitage, 2020). One potential way of explaining this is by assuming that a planet migrates to its final location from farther out in the disk (Dawson & Johnson, 2018).

Once a planet forms in a disk, the planet interacts with the disk and then may migrate inwards or outwards. Planetary migration can be described by two distinct

types: Type I and Type II.

1.5.1 Type I migration

Ward (1997) describes Type I migration due to a non zero net torque on the planet exerted by a disk. The planet drifts relative to the disk on a timescale which is inversely proportional to the mass of the protoplanet. Type I migration relates to low-mass planets (e.g. Earth-mass planets) that are not able to open a gap in the disk.

1.5.2 Type II migration

Ward (1997) also describes Type II migration as when the planet is sufficiently massive enough to open a gap in the disk so that a flow barrier to the disk gas may be established. The planet becomes locked into the disk. As the disk evolves, the protoplanet migrates inwards on a timescale described by the disk's viscosity. The standard Type II migration is in an inward direction, however, with a massive disk it is possible for the planet to move in an outward direction (Stamatellos & Inutsuka, 2018). In a non-standard Type II migration, the planet moves outward due to interactions with the gravitationally unstable gap edges.

1.6 Migration Timescale

Tanaka, Takeuchi & Ward (2002a) assumes that waves excited by a planet in a disk are weak enough for the linear theory to be valid. This is true when the Hill's radius of the planet is smaller than the scale height of the disk. They also assume vertically isothermal disks and that the perturbations are isothermal.

Type I migration is defined as a change in the planet's orbit as a result of the total torque exerted on the planet from the disk. This torque is given by (Armitage,

2020),

$$T_{\rm Planet} = \sum_{\rm ILR} T_{\rm LR} + \sum_{\rm OLR} T_{\rm LR} + T_{\rm CR}, \tag{1.4}$$

where ILR is the inner Lindblad resonances and OLR is the outer Lindblad resonances, with the planet gaining angular momentum from the ILR and losing angular momentum to the OLR. $T_{\rm CR}$ is the co-rotational torque and is given by (Tanaka, Takeuchi & Ward, 2002b),

$$T_{\rm CR} = -\left(1.36 - 0.54\gamma\right)\left(\frac{M_{\rm P}}{M_*}\frac{r_{\rm P}\,\Omega_{\rm P}}{c_{\rm s}}\right)^2 \Sigma_{\rm P}\, r_P^4\, \Omega_{\rm P}^2, \tag{1.5}$$

where $M_{\rm P}$ is the mass of the planet, M_* is the mass of the star, $r_{\rm P}$ is the orbital radius of the planet, $\Sigma_{\rm P}$ is the gas surface density, $c_{\rm s}$ is the gas sound speed and $\Omega_{\rm P}$ is the angular velocity at $r_{\rm P}$, given as (Papaloizou & Larwood, 2000),

$$\Omega_{\rm P} = \sqrt{\frac{G\,M_*}{r^3}}. \tag{1.6}$$

The net torque, $\rm T_{LR}$, for a disk with surface density $\Sigma(\rm r) \propto \rm r^{-\gamma}$ is given by (Tanaka, Takeuchi & Ward, 2002a),

$$T_{\rm LR} = -\left(2.34 - 0.1\gamma\right)\left(\frac{M_{\rm P}}{M_*}\frac{r_{\rm P}\,\Omega_{\rm P}}{c_{\rm s}}\right)^2 \Sigma_{\rm P}\, r_{\rm P}^4\, \Omega_{\rm P}^2. \tag{1.7}$$

The migration timescale for Type I migration is given by (Armitage, 2020),

$$\tau_{\rm I} = \frac{M_{\rm P}\, v_{\rm P}\, r_{\rm P}}{T_{\rm P}}, \tag{1.8}$$

where $T_{\rm P}$ is the torque exerted on the planet and $v_{\rm P}$ is the orbital velocity of the planet.

As the outer Lindblad resonances are stronger, the migration is inwards. The migration timescale is (Tanaka, Takeuchi & Ward, 2002a),

$$\tau_{\rm I,LR} = \left(2.34 - 0.1\gamma\right)^{-1} \frac{1}{M_{\rm P}}\frac{M_*^2}{\Sigma_{\rm P}\, r_{\rm P}^2}\left(\frac{c_{\rm s}}{r_{\rm P}\,\Omega_{\rm P}}\right)^2 \Omega_{\rm P}^{-1}. \tag{1.9}$$

The timescale for standard (inward) Type II migration is (Armitage, 2020),

$$\tau_{\rm II} = \frac{2}{3\,\alpha}\left(\frac{h}{r}\right)_{\rm P}^{-2} \Omega_{\rm P}^{-1}. \tag{1.10}$$

Here, h and r are the disc scale height of the planet and the orbital radius of the planet, respectively and α is the viscosity parameter.

1.7 Thesis outline

The aim of this project is to investigate the orbital migration of gas giant planets embedded in massive circumbinary disks on wide orbits. The classical planet formation theory (CA) is challenged by the observed locations of wide orbit gas giant planets. Giant planets forming on wide orbits through core accretion is not plausible due to the long formation timescale of the process, i.e. a few Myr. It is possible that these planets form through disk instability as the formation timescale for planets is much shorter, i.e. a few 10^3 yr (Dawson & Johnson, 2018). The problem that arises is that a planet embedded in a massive disk will migrate quickly inwards (Baruteau, Meru & Paardekooper, 2011). However, migration in massive disks may happen on an outward direction (Stamatellos & Inutsuka, 2018). This is the main topic of our study. More specifically we aim to study migration in massive disks around binary stars.

We perform a set of simulations of planet migration in massive circumbinary disks and analyse the results. We describe the initial conditions of the disk and an overview of Smooth Particle Hydrodynamics (SPH) in Chapter 2. In Chapter 3, we discuss the benchmark run, convergence and the settling of the disk. We discuss the migration of the planet in a disk around binary stars with varying parameters in Chapter 4. Finally, in Chapter 5 we discuss the role that each binary variable has on the migration of the planet and summarize our results.

Chapter 2

Computational Methods

2.1 Smooth Particle Hydrodynamics

We will simulate the dynamics of giant planets in gaseous disks using SEREN, a Smoothed Particle Hydrodynamics (SPH) code developed by Hubber et al. (2011). Gingold & Monaghan (1977) and Lucy (1977) first introduced the concept of SPH. SPH refers to a computational method in which the equations of hydrodynamics are solved using a large number of particles to represent the fluid. In the specific case of this project, this equates to solving hydrodynamic equations in order to simulate a protostellar disk. SPH uses a smoothing length, h, to smooth the properties of the particles using a weighting function that is referred to as the kernel function. Particles within a specific volume are then allowed to hydro-dynamically interact with other particles.

Monaghan (1992) reviews the hydrodynamic equations using SPH formalism. The SPH momentum equation, or equation of motion, is given by

$$\frac{d\,\vec{v}_{\rm a}}{dt} \,=\, -\sum_{\rm b} m_{\rm b} \left(\frac{P_{\rm a}}{\rho_{\rm a}^2} \,+\, \frac{P_{\rm b}}{\rho_{\rm b}^2} \,+\, \Pi_{\rm ab} \right) \nabla_{\rm a} W_{\rm ab}, \tag{2.1}$$

where $m_{\rm b}$ is the mass of SPH particle b, $P_{\rm b}$ its pressure, $\rho_{\rm b}$ its density, $P_{\rm a}$ the pressure of particle a, $\rho_{\rm a}$ its density and $\nabla_{\rm a}{\rm W}_{\rm ab}$ the gradient of the interpolating

kernel taken with respect to particle a. Artificial viscosity is included through the term (Stamatellos et al., 2007a)

$$\Pi_{\rm ab} \, = \, \left\{ \begin{array}{cc} -\alpha_{\rm SPH} \frac{\bar{c}_{\rm S,ab} \mu_{\rm ab}}{\bar{\rho}_{\rm ab}} \, + \, \beta_{\rm SPH} \, \frac{\mu_{\rm ab}^2}{\bar{\rho}_{\rm ab}} & {\rm if} \mu_{\rm ab} < 0 \\ 0 & {\rm otherwise} \end{array} \right\}, \tag{2.2}$$

where $\alpha_{\rm SPH}$ and $\beta_{\rm SPH}$ are the SPH viscosity coefficients, $\mu_{\rm ab}$ is the velocity field divergence and $\bar{c}_{\rm S,ab}$ is the averaged sound speed. The spatial resolution of the simulation is determined by the smoothing length and has a direct effect on the viscosity, α_{SS} (Shakura & Sunyaev, 1973) of the system,

$$\alpha_{\rm SS} \, \approx \, \frac{1}{10} \, \alpha^{\rm SPH} \, \frac{\langle h \rangle}{H}, \tag{2.3}$$

where $\langle h \rangle$ refers to the mean smoothing length of SPH particles at a given radius and H is the disk scale height. The coefficient used in this equation, $\frac{1}{10}$, is sensitive to the smoothing kernel. Reducing the smoothing length increases the resolution of the simulation. However, doing so requires a larger number of particles in the simulation (to preserve the number of particles within one smoothing length) and leads to a decreased viscosity within the system.

The second equation needed when simulating SPH is the energy equation and is given by

$$\frac{du_{\rm a}}{dt} \, = \, \frac{1}{2} \sum_{\rm b} m_{\rm b} \left(\frac{P_{\rm a}}{\rho_{\rm a}^2} \, + \, \frac{P_{\rm b}}{\rho_{\rm b}^2} \, + \, \Pi_{\rm ab} \right) \vec{v}_{\rm ab} \, \cdot \, \nabla_{\rm a} \, W_{\rm ab}, \tag{2.4}$$

where $\vec{v}_{\rm ab}$ is the velocity difference $\vec{v}_{\rm a} \, - \, \vec{v}_{\rm b}$ for particles a and b. Finally, the third equation is the continuity equation and is given by

$$\frac{d\rho_{\rm a}}{dt} \, = \sum_{\rm b} m_{\rm b} \, \vec{v}_{\rm ab} \, \cdot \, \nabla_{\rm a} \, W_{\rm ab}. \tag{2.5}$$

These equations are integral in allowing the 3D SPH code SEREN to simulate the various systems in this project.

2.2 Initial Conditions

It is the intention of this project to model a gas giant planet, of mass $M_{\rm P} = 1\,{\rm M_J}$, embedded in a protoplanetary disk of mass $M_{\rm Disk} = 0.1\,{\rm M_\odot}$. This disk will initially be modelled around a single star of mass $M_* = 1\,{\rm M_\odot}$, before being modelled around a binary system. The parameters of this disk and planet system are taken from Stamatellos & Inutsuka (2018), with the later binary parameters being varied to investigate their effect on the migration of the planet. The disk is constructed by setting its surface density, temperature, etc.

2.2.1 Disk surface density profile

The surface density profile assumed here is given by

$$\Sigma\,(R) \;=\; \Sigma_0 \left(\frac{R_0^2}{R_0^2 \,+\, R^2}\right)^{\frac{\rm p}{2}}, \tag{2.6}$$

where Σ_0 is the surface density at $\rm R = 0$, R is the distance from the star and R_0 is the softening radius. Semi-analytical and theoretical studies of cloud collapse and subsequent disk formation (e.g., Lin & Pringle, 1990) suggest that $\Sigma(R) \sim R^{-\rm p}$ where p is between 1 and $\frac{3}{2}$.

2.2.2 Disk temperature

The two processes that determine the disk temperature are irradiation from the central star and viscous dissipation which generates energy. For the case in which the disk temperature changes through irradiation at a distance R, the flux scales as $\frac{1}{R^2}$ and the incident angle on the disk surface scales as $\frac{1}{R}$. Therefore, the total radiation on the disk scales as $\frac{1}{R^3}$. For the case in which the disk is heated by viscous dissipation, the angular momentum between parts of the disk with different angular velocities is the defining factor. For both cases, the temperature varies as $R^{-\frac{3}{4}}$. However, for the viscous dissipation case the proportionality is determined

by the mass of the star and the mass accretion rate. For the case of irradiation, this proportionality constant is determined by the luminosity of the star. The disk temperature in this work is set using a general profile and is given by

$$T_{\mathrm{d}}\left(R\right) = \left[T_0^2 \left(\frac{R^2 + R_0^2}{\mathrm{AU}^2}\right)^{-\mathrm{q}} + T_\infty^2\right]^{\frac{1}{2}}, \tag{2.7}$$

where T_0 is the temperature at R = 1AU, T_∞ is the temperature at an extreme distance from the star and q is assumed to be q = 0.5.

2.2.3 Disk thickness

Protostellar disks are flared towards their outer edges with the thickness increasing linearly from the star. For more massive disks the flare is much less pronounced than it would be for low mass disks. The thickness of the disk can be calculated by equating the gravitational force of the disk and the vertical component of the gravitational force of the star, against the disk thermal pressure

$$\frac{G\,M_*}{R^2}\,\frac{z_0\left(R\right)}{R} + \pi\,G\,\Sigma\left(R\right) \approx \frac{c_{\mathrm{s}}^2\left(R\right)}{z_0\left(R\right)}, \tag{2.8}$$

where z_0 is the thickness of the disk and $c_{\mathrm{s}}\left(R\right)$ is the local sound speed. This equation can be rewritten as

$$\frac{G\,M_*}{R^3}\,z_0^2\left(R\right) + \pi\,G\,\Sigma\left(R\right)\,z_0\left(R\right) - c_{\mathrm{s}}^2\left(R\right) = 0. \tag{2.9}$$

This equation is simply a quadratic with a positive root

$$z_0\left(R\right) = -\frac{\pi\,\Sigma\left(R\right)\,R^3}{2\,M_*} + \left[\left(\frac{\pi\,\Sigma\left(R\right)\,R^3}{2\,M_*}\right)^2 + \frac{R^3}{G\,M_*}\,c_{\mathrm{s}}^2\left(R\right)\right]^{\frac{1}{2}}. \tag{2.10}$$

2.2.4 Disk rotation

It is assumed that the disk rotates with constant velocity v at a distance R from the central star. The centrifugal force is due to the gravity of the star and the

self-gravity of the disk, so the initial velocity of the disk can be calculated using

$$v = \left[\frac{G\,[M_* + M_{\rm disk}\,(< R)]}{R}\right]^{\frac{1}{2}}, \tag{2.11}$$

where $M_{\rm disk}\,(< R)$ is the mass of the disk interior to radius R. This is a good approximation of the velocity field in self-gravitating disks.

2.3 Sinks

The star and planet are represented by sink particles and will only interact with the rest of the computational domain through their gravity (Bate, Bonnell & Price, 1995). The sink radius of the star and planet is chosen as $\mathrm{R_{sink,*}} = 0.2\,\mathrm{AU}$ and $\mathrm{R_{sink,P}} = 0.1\,\mathrm{AU}$, respectively. The sink radius of the planet was chosen so that it is smaller than its Hill radius. The Hill radius is the region in which the gravity of the planet dominates the gravity of star and is given by

$$R_{\rm H} = \left(\frac{1\,M_{\rm P}}{3\,M_*}\right)^{\frac{1}{3}} R, \tag{2.12}$$

where $M_{\rm P}$ is the mass of the planet, M_* is the mass of the star and R is the orbital radius. For a planet of mass $M_{\rm P} = 1\,\mathrm{M_J}$ that orbits a solar mass star at $\alpha = 50\,\mathrm{AU}$, the Hill radius is $R_{\rm H} = 3.4\,\mathrm{AU}$. This value will change as the planet accretes material from the disk and migrates over time.

2.4 Disk thermodynamics

The disk thermodynamics are generally described either using the β - cooling method or more detailed radiative transfer (Mercer, Stamatellos & Dunhill, 2018). Baruteau, Meru & Paardekooper (2011) discuss the impact of β cooling on the migration of Jupiter-mass planet's in massive protoplanetary disks. They find that the Jupiter-mass planet is able to migrate inwards from 100 AU to 20 AU in less than 10 orbits.

This time-scale is shorter than the gap-opening time-scale and therefore the planet does not switch to Type II migration.

For this project, we use the approximate radiative transfer method as in Stamatellos (2015). Stamatellos et al. (2007b) discusses the implementation of the radiative transfer method and describes how the method uses the density, gravitational potential and temperature of each SPH particle to estimate the mean optical depth. This mean optical depth regulates not only the cooling of each particle but also its heating as well. The net radiative heating/cooling for SPH particle i is given by

$$\frac{du_{\rm i}}{dt}\,|_{\rm RAD} = \frac{4\,\sigma_{\rm SB}\,\left(T_{\rm A}^4\,-\,T_{\rm i}^4\right)}{\overline{\Sigma}_{\rm i}^2\,\overline{\kappa}_{\rm R}\left(\rho_{\rm i},\,T_{\rm i}\right)\,+\,\kappa_{\rm P}^{-1}\left(\rho_{\rm i},\,T_{\rm i}\right)}, \tag{2.13}$$

where $\sigma_{\rm SB}$ is the Stefan-Boltzmann constant, $\overline{\Sigma}$ is the mass-weighted mean column density, $\overline{\kappa}_{\rm R}$ and $\kappa_{\rm P}$ are the Rosseland- and Planck-mean opacities. $T_{\rm A}$ is the pseudo-background radiation temperature and is given by Equation 2.7.

2.4.1 Initial conditions of the binary systems

For binary systems, the initial conditions of the planet and disk will be the same as simulations of single star systems. However, additional parameters will be present. These include the initial binary mass, separation and eccentricity.

Chapter 3

Planetary migration in a disk around a single solar mass star

3.1 Initial conditions of the benchmark run

In this chapter, the simulation of a $1\,\mathrm{M_J}$ planet orbiting a $1\,\mathrm{M_\odot}$ star at an initial semi-major axis of 50 AU is described. The orbit of the planet is initially circular, therefore the eccentricity is $e = 0$. This planet is embedded in a $0.1\,\mathrm{M_\odot}$ disk with inner radius $R_{\mathrm{D,\,In}} = 0.2\,\mathrm{AU}$ and outer radius $R_{\mathrm{D,\,Out}} = 100\,\mathrm{AU}$. The disk is settled for 3 kyr before the planet is embedded within it. The planet is then allowed to evolve within the disk for 20 kyr. These parameters are based on those of Stamatellos & Inutsuka (2018) to allow for comparisons to be made. In this chapter, topics such as settling the disk and convergence will be covered as to inform the parameters of the benchmark run.

3.1.1 Convergence

We perform nine simulations using a varying number of SPH particles to represent a disk that has been settled for 3 kyr to check for convergence (see Fig 3.1). The

number of SPH particles used are $0.5\,\mathrm{x}\,10^5$, $1\,\mathrm{x}\,10^5$, $2\,\mathrm{x}\,10^5$, $2.5\,\mathrm{x}\,10^5$, $3\,\mathrm{x}\,10^5$, $4\,\mathrm{x}\,10^5$, $5\,\mathrm{x}\,10^5$ and $6\,\mathrm{x}\,10^5$. Our aim is to find how many particles we need to use to reproduce the results of Stamatellos & Inutsuka (2018), which uses $10\,\mathrm{x}\,10^5$ SPH particles to represent the disk.

It can be seen that two trends emerge with regards to the semi-major axis of the planet (see Fig 3.1a). In the simulations that use below $3\,\mathrm{x}\,10^5$ SPH particles the planet migrates inwards and the results diverge from those of Stamatellos & Inutsuka (2018), whereas in the simulations using more than $4\,\mathrm{x}\,10^5$ the results from this paper are reproduced. Therefore convergence is achieved above $4\,\mathrm{x}\,10^5$ SPH particles.

It can be seen in Fig 3.1a that Type I migration continues for a further ~ 0.5 kyr in Stamatellos & Inutsuka (2018) simulation compared to the $5\,\mathrm{x}\,10^5$ SPH particle simulation. However, this only leads to a difference of 4 AU in the semi-major axis of the planet at the end of the run (20 kyr) between the two simulations which equates to an 8% difference. Once Type II migration becomes dominant, a similar relationship is seen with a 8% difference between the two semi-major axes. This gives confidence in the benchmark run simulation. With such a similar output given by both the benchmark run and Stamatellos & Inutsuka (2018), it can be inferred that an increase in SPH particle number would only lead to small differences between the two. Therefore, there is little value of increasing the number of SPH particles further. We therefore choose $5\,\mathrm{x}\,10^5$ SPH particles for the simulations for this project.

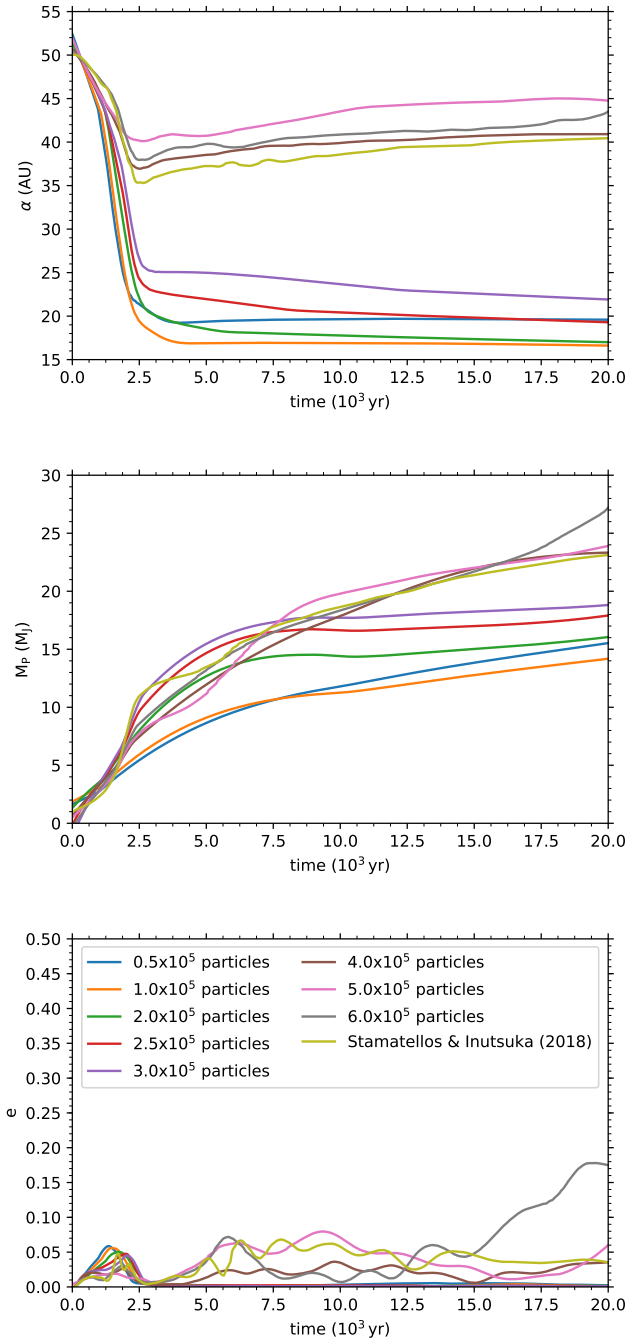

Figure 3.1: A comparison of $0.5\,\mathrm{x}\,10^5$, $1\,\mathrm{x}\,10^5$, $2\,\mathrm{x}\,10^5$, $2.5\,\mathrm{x}\,10^5$, $3\,\mathrm{x}\,10^5$, $4\,\mathrm{x}\,10^5$, $5\,\mathrm{x}\,10^5$, $6\,\mathrm{x}\,10^5$ and $10\,\mathrm{x}\,10^5$ SPH particle simulations. The $10\,\mathrm{x}\,10^5$ SPH particle simulation is data taken from Stamatellos & Inutsuka (2018). This plot shows the evolution of the planet's (a) semi-major axis (b) mass and (c) eccentricity over a period of 20 kyr (top to bottom).

3.1.2 Settling the disk

To model planetary systems, the disk must first be allowed to relax. If the system is not allowed to relax then the evolving disk will affect the orbital evolution of the planet. A disk is settled when its surface density has reached a value that does not change significantly with time. As the disk settles a perturbation can be seen in its surface density profile that is effectively a wave travelling from the centre of the disk outwards.

To check for how long we need to allow the disk to relax before embedding the planet, we perform simulations with different disk settling times, 2, 3, and 5 kyr that correspond to 2, 3 and 5 outer rotational periods at 100 AU.

Fig 3.2 compares the evolution of the planet properties for disks relaxed for 2 kyr, 3 kyr and 5 kyr. When looking at the semi-major axis of the planets, it can be seen that the simulations with the three relaxation times are extremely similar. The smallest semi-major axis of the planet, is between 38 AU and 42 AU. Their final, maximum semi-major axis, are similar with values between 42 AU and 48 AU. The mass of the planet evolves with similar trends for each disk relaxation period. The largest diversion between the three is the final value for a disk relaxed for 5 kyr but this is a small difference of 2 M_J after 20 kyr, which is aound $\sim 10\,\%$. We therefore chose to relax the disks in our simulations for 3 kyr.

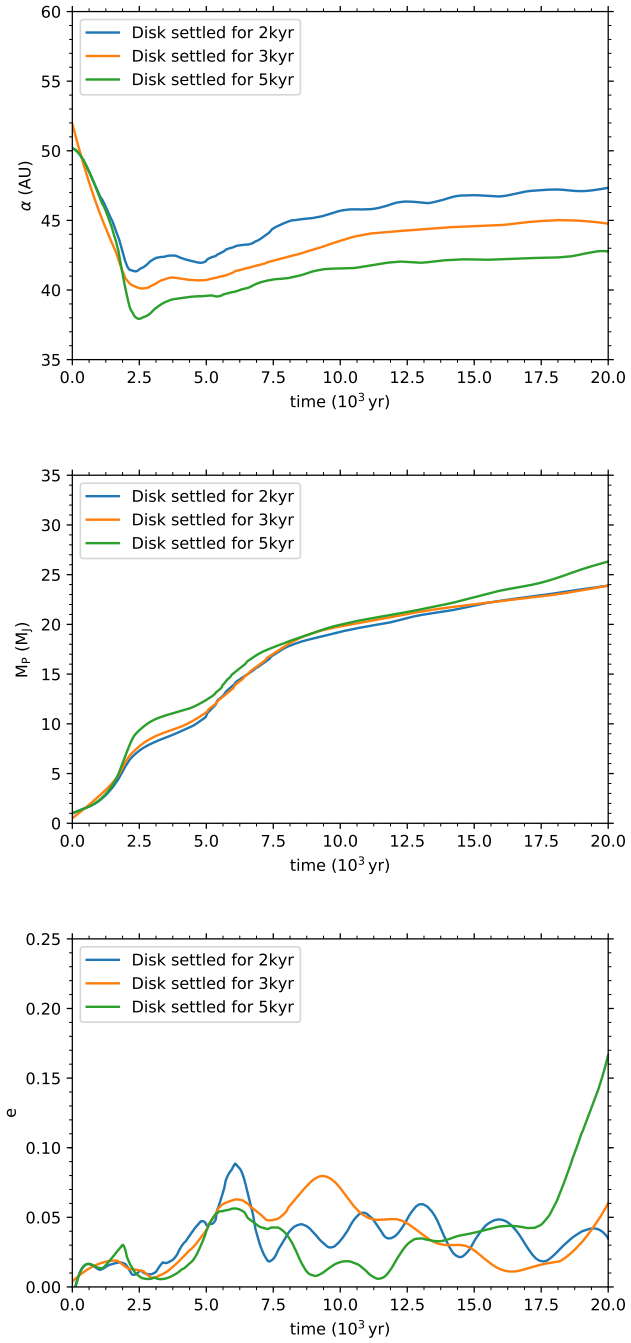

Figure 3.2: A comparison of simulations with disks relaxed for 2 kyr, 3 kyr and 5 kyr. Here the (a) semi-major axis (b) mass and (c) eccentricity of the planet are shown as it evolves for 20 kyr.

3.2 Benchmark run

We define the 'benchmark run' to be used for comparisons as follows: a $1\,M_J$ planet, with a semi-major axis of 50 AU, embedded in a $0.1\,M_\odot$ disk surrounding a single $1\,M_\odot$ star. The initial orbit is circular, i.e. $e = 0$, and the disk extends from 0.1 AU to 100 AU. The surface density of the disk follows Equation 2.6, where $p = 1$ and Σ_0 is determined from the disk mass. The temperature profile of the disk follows Equation 2.7 where $q = 0.5$ and $T_0 = 250\,K$. The disk is modelled with 5×10^5 SPH particles and allowed to relax for three outer orbits (3 kyr). After the planet is embedded within the disk, the system is evolved for a further 20 kyr. The surface density of the disk at different instances during its evolution are show in Fig 3.3. The planet migrates inwards initially, opens up a gap and then starts migrating outwards.

Fig 3.4a shows the evolution of the planet's semi-major axis over a period of 20 kyr. The planet rapidly migrates inwards over a period of 2.5 kyr until it reaches a minimum of 40 AU. This trend is similar to that of Type I migration, primarily seen with low-mass planets embedded in low-mass disks. A trend such as this indicates a strong interaction between the disk and planet. The formation of a gap can be seen in Fig 3.3 at $t = 2$ kyr, which indicates a change in migration to a Type II migration. However, as the planet migrates in an outward direction this is a non-standard form of Type II migration. The planet migrates outwards because it gains angular momentum from outside its orbit. This can be further seen in Fig 3.4, after the initial rapid inward migration a slow outward migration follows which is a clear indication of non-standard Type II migration.

Fig 3.4b shows the evolution of the planet's mass over a period of 20 kyr. The initial mass of the planet was set to $1\,M_J$ and the planet attains a final mass of $24\,M_J$ which is comparable to that of Stamatellos & Inutsuka (2018). Stamatellos & Inutsuka (2018) find a final mass of $23\,M_J$ which has a difference of only 4% from our

benchmark run. Fig 3.4c shows the planet's eccentricity over the evolutionary period. The planet in our benchmark run follows a similar trend to that of Stamatellos & Inutsuka (2018) with minor differences attributed due to the random change of the planet's eccentricity as it interacts with the disk.

Fig 3.5 shows the Toomre parameter, temperature and surface density of the disk. The surface density of the disk (see Fig 3.5a) shows a peak at 15 AU before decreasing. The temperature of the disk (see Fig 3.5b) decreases exponentially as expected. Finally as seen in Fig 3.5c, the Toomre parameter is above 1 but between 1 - 2 for a wide range of distances from the central star, indicating the disk is marginally unstable. A planet evolving in such a disk is expected to initially migrate inwards and then slightly migrate outwards, as the planet interacts with gravitationally unstable gap edges (Lin & Papaloizou, 2012; Stamatellos & Inutsuka, 2018).

Table 3.1 shows the semi-major axis α, migration timescale $\tau_{\rm mig}$, mass $M_{\rm P}$ and migration velocity $v_{\rm mig}$ of the planet at different times during the evolution of the system. The values present in this table are calculated at five specific times. The migration timescale is calculated using

$$\tau_{\rm mig} = \frac{\alpha}{\frac{d\alpha}{dt}}, \tag{3.1}$$

and the migration velocity using

$$v_{\rm mig} = \frac{d\alpha}{dt}. \tag{3.2}$$

Here it can be seen that the planet's migration timescale increases over the course of the simulation, which is expected. Two of the time instances chosen show an outward migration, which is denoted by the minus sign. The magnitude of the migration velocity is larger initially during the time when the planet undergoes Type I migration. Type I migration has a shorter migration timescale than that of Type II migration (for a $1\,{\rm M_J}$ planet), and therefore the migration velocity would be higher as a result. The values for migration velocity are comparable to that of

Stamatellos & Inutsuka (2018), showing only minor differences such as the direction of migration at 2.5 kyr. The migration timescale values follow a similar trend to that of Stamatellos & Inutsuka (2018). However, at 2.5 kyr the benchmark run shows a negative value compared to the positive value of Stamatellos & Inutsuka (2018), indicating that the planet has started migrating outwards a bit sooner.

Table 3.1: Semi-major axis α, migration timescale $\tau_{\rm mig}$, planet mass $M_{\rm P}$ and migration velocity $v_{\rm mig}$ for the benchmark run. Here, the negative values indicate the planet is migrating in an outward direction.

t (kyr)	α (AU)	$\tau_{\rm mig}$ (kyr)	$M_{\rm P}$ ($M_{\rm J}$)	$v_{\rm mig}$ (AU/kyr)
0.7	48.2	9.7	2.0	5.1
1.5	43.8	11.0	4.1	4.0
2.5	40.0	-23.9	8.2	-1.7
5	40.6	-269.0	11.8	-0.2
18	45.0	425.0	24.1	0.1

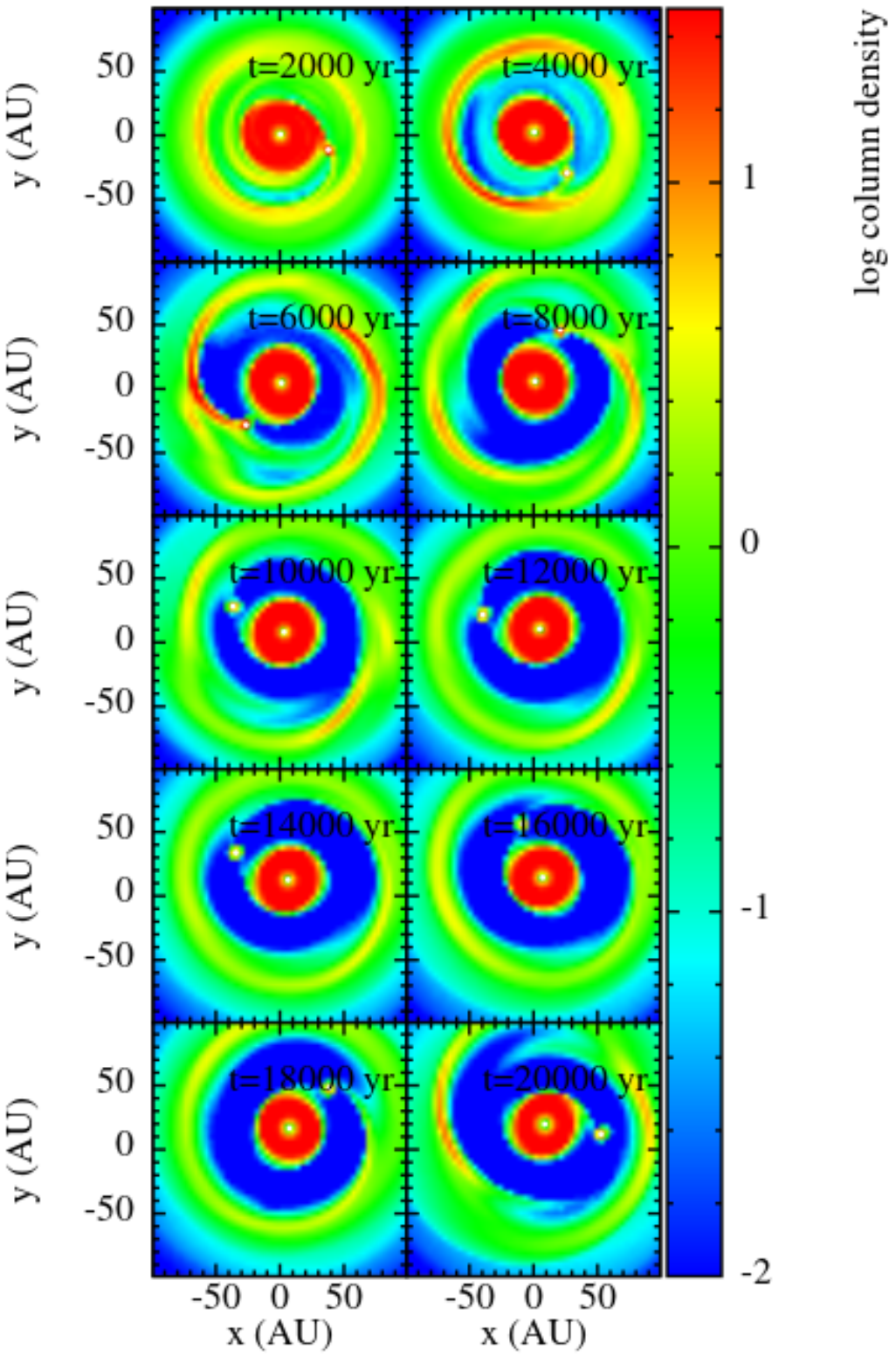

Figure 3.3: The evolution of the surface density of the disk for the benchmark run: $1\,M_J$ planet embedded in a $0.1\,M_\odot$ disk (represented by 5×10^5 SPH particles) around a $1\,M_\odot$ star as it evolves for 20 kyr.

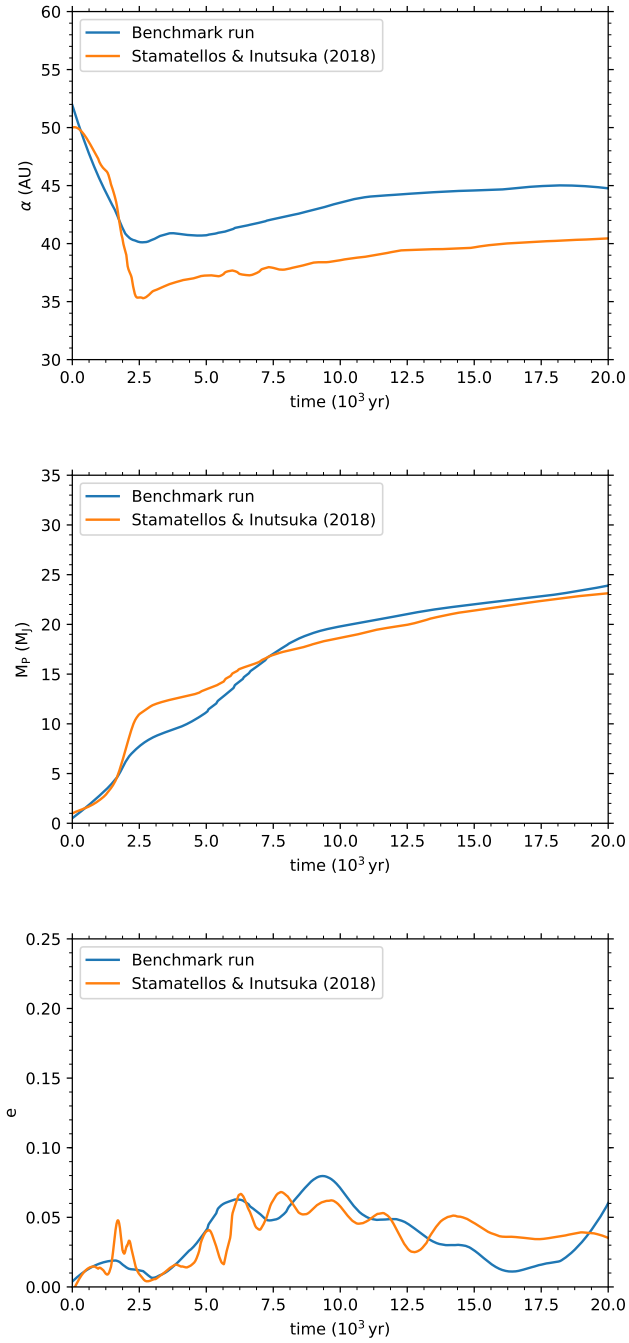

Figure 3.4: The evolution of the (a) semi-major axis (b) mass and (c) eccentricity of a $1\,M_J$ planet embedded in a $5\,x\,10^5$ SPH particle disk orbiting a $1\,M_\odot$ star (the benchmark run). We also compare this run with that from Stamatellos & Inutsuka (2018).

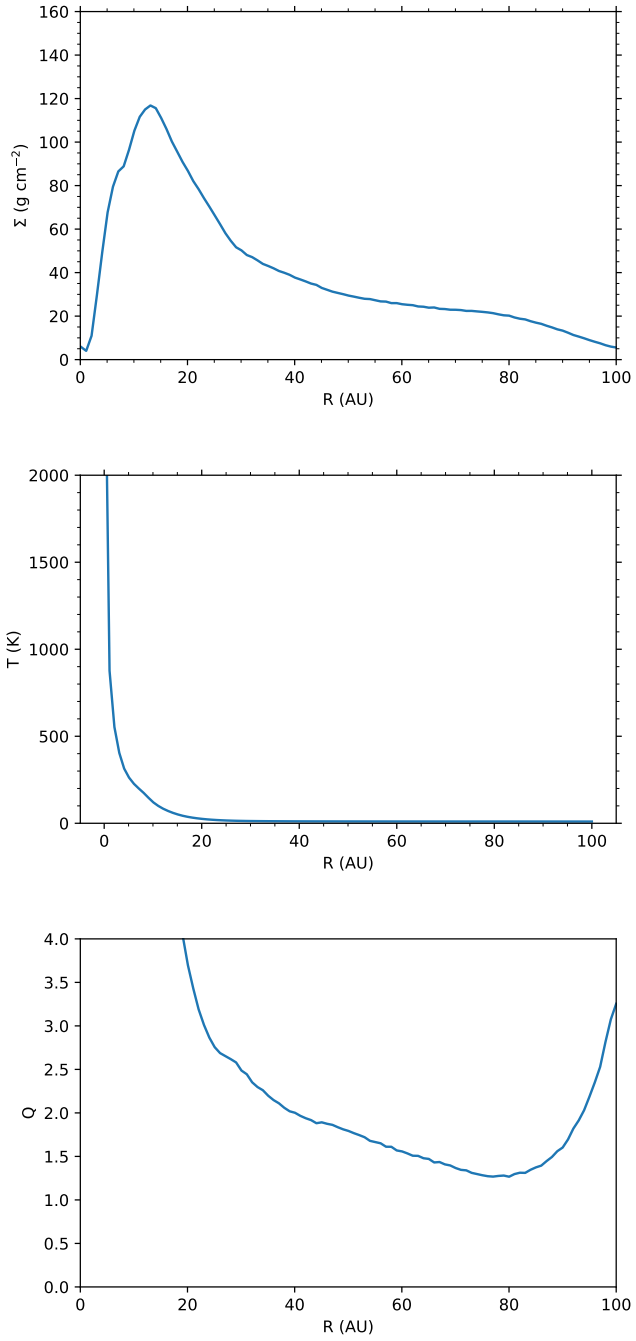

Figure 3.5: The initial surface density(top), the temperature profile (middle), and Toomre parameter (bottom) of the disk for the benchmark run.

Chapter 4

Planetary migration in a disk around a binary system

We now examine how a planet will migrate in a disk around a binary system and how this migration compares to migration around a single star. We keep the disk parameters (i.e. surface density, temperature profile and mass) and the planet parameters (i.e. semi-major axis of the planet) the same as in the benchmark run. In this section we investigate how the binary parameters (binary mass, separation, eccentricity) affect the evolution of the planet's orbit. In the ten runs presented here, the planet is initially placed at 50 AU with a circular orbit within a $0.1\,M_{\odot}$ circumbinary disk represented by 5×10^5 SPH particles. As with the benchmark run, the disk extends from 0.1 AU to 100 AU and has been relaxed for 3 kyr. This allows for comparisons to be made between these simulations and the benchmark run.

Table 4.1: The ten simulations run for this project, with the binary parameters listed.

Run	Stellar Masses ($M_\odot$)	Binary Separation α_b (AU)	Eccentricity e_b
1	0.5 - 0.5	1	0
2	0.5 - 0.5	1	0.2
3	0.5 - 0.5	5	0
4	0.5 - 0.5	5	0.2
5	0.5 - 0.5	5	0.5
6	0.8 - 0.2	1	0
7	0.8 - 0.2	1	0.2
8	0.8 - 0.2	5	0
9	0.8 - 0.2	5	0.2
10	0.8 - 0.2	5	0.5

Table 4.1 shows the parameters varied in this projected for the binary systems simulated. We choose the total mass of the binary system to be $1\,M_\odot$, i.e. the same as in the single star runs. We made sure that parameters that result in disk disruption (e.g. fragmentation) has been avoided. In each of the runs above, the disk remained undisrupted during the 20 kyr of the simulation. Combinations such as an initial binary separation of $\alpha_b = 1$ AU and an eccentricity of $e_b = 0.5$, which led to the planet being ejected from the system shortly after the start of the simulation, were not included in this study. In the following sections we describe in detail the results from each run.

4.1 Run 1: 0.5 - 0.5 $M_\odot$, $\alpha_b = 1$ AU, $e_b = 0$

Fig 4.1 shows the evolution of the semi-major axis, mass and eccentricity of the planet over a period of 20 kyr. As seen in Fig 4.1a, the planet undergoes Type I migration reaching a semi-major axis of 41 AU. This is comparable to the minimum semi-major axis of the benchmark run (a difference of 2%). Once a gap in the disk forms at t = 2 kyr, the migration changes to a non-standard Type II outward migration. As a result of the non-standard Type II migration, the planet's semi-major axis reaches 47 AU which is a 4% increase on the benchmark run. The evolution of the planet's mass (see Fig 4.1b) shows an almost identical trend to that of the benchmark run reaching a value of $M_P = 24\,M_J$ (a difference of 2%). The evolution of the planet's eccentricity (see Fig 4.1c) follows a similar trend to the benchmark run, reaching a final eccentricity of 0.02.

Table 4.2 shows the migration timescale, mass and migration velocity of the planet over the course of its evolution. It can be seen that the planet follows a similar trend to that of the benchmark run with regards to its inward and outward migration pattern. However, the migration timescale shows a significant difference at the end of the run (by a factor of 10). This shows the impact of a binary system with a small binary separation and zero eccentricity on the planet.

Table 4.2: The semi-major axis α, migration timescale $\tau_{\rm mig}$, mass $M_{\rm P}$ and migration velocity $v_{\rm mig}$ of the planet at different times, for Run 1. The binary consists of two $0.5\,{\rm M}_\odot$ stars, and initially has zero eccentricity $e_{\rm b}=0$ and semi-major axis $\alpha_{\rm b}=1\,{\rm AU}$. Here, the negative values in $v_{\rm mig}$ indicate the planet is migrating in an outward direction.

t (kyr)	α (AU)	$\tau_{\rm mig}$ (kyr)	$M_{\rm P}$ ($\rm M_J$)	$v_{\rm mig}$ (AU/kyr)
0.7	48.3	11.8	1.9	4.2
1.5	44.6	10.5	3.9	4.3
2.5	41.1	-20.6	8.1	-2.0
5	41.6	-104.4	12.3	-0.4
18	46.8	3359.7	24.7	0.01

4.2 Run 2: 0.5 - 0.5 $\rm M_\odot$, $\alpha_{\rm b}=1$ AU, $e_{\rm b}=0.2$

Fig 4.1 shows the evolution of the semi-major axis, mass and eccentricity of the planet over 20 kyr. As seen in Fig 4.1(a), the planet undergoes Type I migration reaching a semi-major axis of 42 AU, a small difference of 5% to the benchmark run. Once a gap in the disk forms at t = 3 kyr, the migration changes to a non-standard Type II outward migration. As a result of the non-standard Type II migration, the planet's semi-major axis reaches 48 AU (a difference of 7% with the benchmark run). The planet's mass (See Fig 4.1b) grows slower than the benchmark run, reaching a value of $M_{\rm P}=23\,{\rm M_J}$. This difference is small, 2%. The evolution of the planet's eccentricity (see Fig 4.1c) follows a similar trend to the benchmark run, reaching a final eccentricity of 0.04.

It can be seen in Table 4.3 that this simulation and the benchmark run also have some differences. For 5 ky and 18 kyr, the values for migration timescale and migration velocity differ by a factor of 10. Table 4.3 (and Fig 4.1a) shows that in

this run the planet moves outwards, then inwards and finally outwards again.

Table 4.3: The semi-major axis α, migration timescale $\tau_{\rm mig}$, mass $M_{\rm P}$ and migration velocity $v_{\rm mig}$ of the planet at different times, for Run 2. The binary consists of two $0.5\,{\rm M}_{\odot}$ stars, and initially has eccentricity $e_{\rm b}=0.2$ and semi-major axis $\alpha_{\rm b}=1\,{\rm AU}$. Here, the negative values in $\tau_{\rm mig}$ and in $\rm v_{mig}$ indicate the planet is migrating in an outward direction.

t (kyr)	α (AU)	$\tau_{\rm mig}$ (kyr)	$M_{\rm P}$ ($\rm M_J$)	$v_{\rm mig}$ (AU/kyr)
0.7	48.3	11.6	1.9	4.4
1.5	45.0	11.3	3.8	4.0
2.5	42.3	-17.7	7.3	-2.4
5	42.3	38.1	10.4	1.1
18	47.6	-76.1	23.7	-0.6

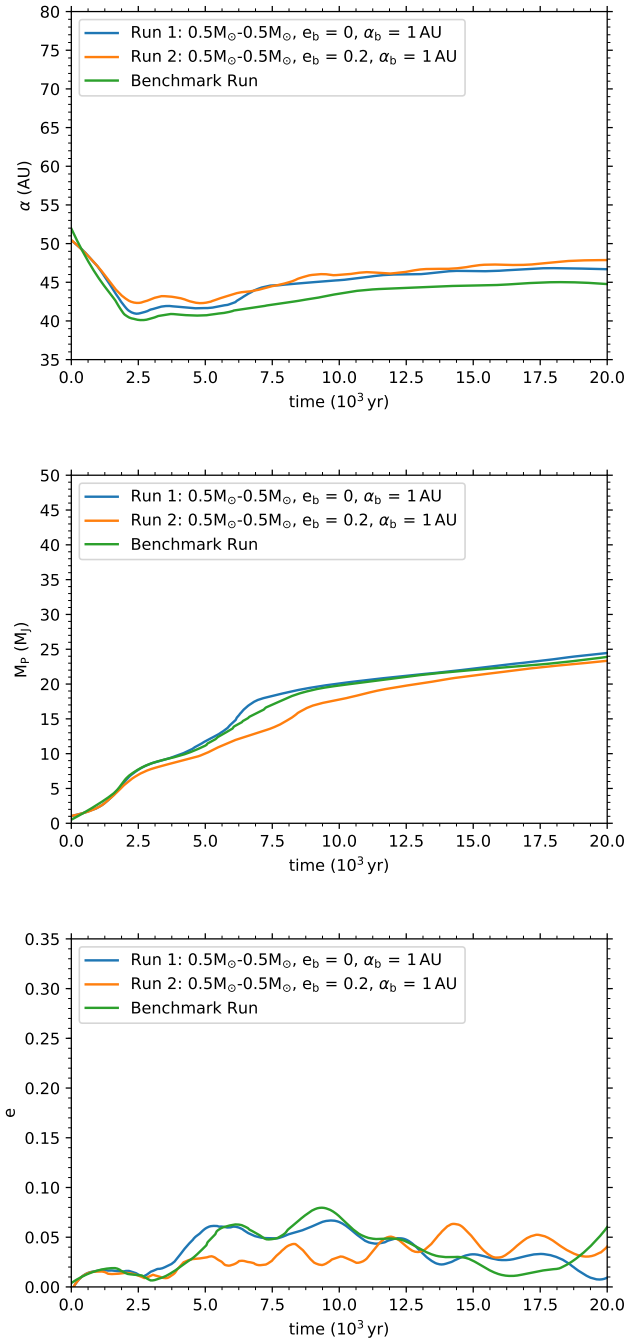

Figure 4.1: $1\,\mathrm{M_J}$ planet embedded in a disk orbiting a binary system consisting of two $0.5\,\mathrm{M_\odot}$ stars, with initial semi-major axis $\alpha_\mathrm{b} = 1\,\mathrm{AU}$ and eccentricity $e_\mathrm{b} = 0$ and $e_\mathrm{b} = 0.2$. (a) The evolution of the semi-major axis of the planet, (b) the evolution of the planet's mass, and (c) the evolution of the planet's eccentricity. The disk modelled here has been settled for 3 kyr.

4.3 Run 3: 0.5 - 0.5 $M_\odot$, $\alpha_b = 5$ AU, $e_b = 0$

Fig 4.2 shows the evolution of the semi-major axis, mass and eccentricity of the planet as it evolves over 20 kyr. The evolution of the semi-major axis of the planet follows a similar trend to that of the benchmark run. Here there is an initial, rapid inward migration that takes place over a comparable time period as the benchmark run, 2.5 kyr. The rapid initial Type I migration reaches a semi-major axis (see Fig 4.2a) of 42 AU a decrease of 6% to that of the benchmark run. Following this there is a period of outward migration followed by inward migration which takes place over the course of 2.5 kyr. Finally there is a non-standard Type II outward migration of the planet, which is more rapid than the benchmark run. At the final phase of evolution the semi-major axis of the planet increases beyond the initial 50 AU, reaching a final value of 54 AU. This final semi-major axis is 8% higher than the initial value and an increase of 19% compared to the benchmark run. The final mass of the planet (see Fig 4.2b) is 32 M_J, almost 30% higher than the final mass of the planet in the benchmark run. The evolution of the planet's eccentricity (see Fig 4.2c) shows a significant increase compared to the benchmark run, reaching a final eccentricity of 0.14.

In a similar capacity to previous binary simulations, Table 4.4 shows similar trends to that of the benchmark run. As before, some notable differences arise with regards to magnitude and direction for the latter times. It can be seen that the migration timescale is significantly shorter than in the benchmark run, reaching a final value that is half that of the benchmark run. However, in this run the planet has a comparable migration velocity to the benchmark run.

Table 4.4: The semi-major axis α, migration timescale $\tau_{\rm mig}$, mass $M_{\rm P}$ and migration velocity $v_{\rm mig}$ of the planet at different times, for Run 3. The binary consists of two $0.5\,{\rm M}_{\odot}$ stars, and initially has eccentricity $e_{\rm b}=0$ and semi-major axis $\alpha_{\rm b}$ =5 AU. Here, the negative values in $v_{\rm mig}$ indicate the planet is migrating in an outward direction.

t (kyr)	α (AU)	$\tau_{\rm mig}$ (kyr)	$M_{\rm P}$ ($\rm M_J$)	$v_{\rm mig}$ (AU/kyr)
0.7	48.3	11.1	1.9	4.4
1.5	44.6	12.3	3.8	3.7
2.5	42.2	-28.5	6.8	-1.5
5	42.4	55.9	10.0	0.8
18	53.1	-251.7	31.1	-0.2

4.4 Run 4: 0.5 - 0.5 $\rm M_{\odot}$, $\alpha_{\rm b}=5$ AU, $e_{\rm b}=0.2$

Fig 4.2 shows the evolution of the planet's semi-major axis, mass and eccentricity over a period of 20 kyr. As seen in Fig 4.2a, the planet undergoes Type I migration reaching a semi-major axis of 42 AU (a difference of 6% to the benchmark run). Once a gap in the disk begins to form at t = 2 kyr, the migration changes to a non-standard Type II outward migration. As a result of the non-standard Type II migration, the planet is able to evolve to a semi-major axis of 58 AU (a difference of 26%). The planet's mass (see Fig 4.2b) reaches a value of $M_{\rm P}=33\,{\rm M_J}$ which is a 31% increase on the benchmark run. The evolution of the planet's eccentricity (see Fig 4.2c) shows a significant increase compared to the benchmark run, reaching a final eccentricity of 0.19.

Table 4.5 also shows differences to the benchmark run. The migration timescale is shorter by a factor of 10 in the latter two times. However, the migration velocity is comparable with that of the benchmark run.

Table 4.5: The semi-major axis α, migration timescale $\tau_{\rm mig}$, mass $M_{\rm P}$ and migration velocity $v_{\rm mig}$ of the planet at different times, for Run 4. The binary consists of two $0.5\,{\rm M}_{\odot}$ stars, and initially has eccentricity $e_{\rm b}=0.2$ and semi-major axis $\alpha_{\rm b}$ =5 AU. Here, the negative values in $v_{\rm mig}$ indicate the planet is migrating in an outward direction.

t (kyr)	α (AU)	$\tau_{\rm mig}$ (kyr)	$M_{\rm P}$ ($\rm M_J$)	$v_{\rm mig}$ (AU/kyr)
0.7	48.3	11.7	1.9	4.2
1.5	44.6	11.9	3.8	3.8
2.5	42.6	-27.3	7.1	-1.5
5	42.6	80.4	9.9	0.5
18	55.3	-56.6	30.8	-1.0

4.5 Run 5: 0.5 - 0.5 $\rm M_{\odot}$, $\alpha_{\rm b}=5$ AU, $e_{\rm b}=0.5$

Fig 4.2 shows the evolution of the planet's, mass and eccentricity over a period of 20k yr. As seen in Fig 4.2a, the planet undergoes Type I migration reaching a semi-major axis of 42 AU, an increase of 6% on the benchmark run. Once a gap in the disk begins to form at t = 2 kyr, the migration changes to a non-standard Type II outward migration. As a result of the non-standard Type II migration, the planet's semi-major axis reaches 71 AU which is a significant increase on the benchmark run (46% higher). The planet's mass (see Fig 4.2b) reaches a value of $M_{\rm P}=39\,{\rm M_J}$ which like with the semi-major axis, is significantly higher than the benchmark run being an increase of 47%. The evolution of the planet's eccentricity (see Fig 4.2c) shows a significant increase compared to the benchmark run, reaching a final eccentricity of 0.22.

Table 4.6 presents an interesting comparison to the benchmark run due to several key differences. While the semi-major axis, mass and eccentricity show a significant

increase on the benchmark run, the migration timescale is shown to be ten times shorter except at 2.5 kyr which is much longer than the benchmark run. The migration velocity is also a magnitude higher at several times.

Table 4.6: The semi-major axis α, migration timescale $\tau_{\rm mig}$, mass $M_{\rm P}$ and migration velocity $v_{\rm mig}$ of the planet at different times, for Run 5. The binary consists of two $0.5\,{\rm M}_{\odot}$ stars, and initially has eccentricity $e_{\rm b}=0.5$ and semi-major axis $\alpha_{\rm b}$ =5 AU. Here, the negative values in $v_{\rm mig}$ indicate the planet is migrating in an outward direction.

t (kyr)	α (AU)	$\tau_{\rm mig}$ (kyr)	$M_{\rm P}$ ($\rm M_J$)	$v_{\rm mig}$ (AU/kyr)
0.7	48.0	9.3	1.9	5.3
1.5	44.5	12.6	3.7	3.6
2.5	43.2	-376.7	6.2	-0.1
5	48.3	42.0	14.1	1.2
18	68.2	-31.9	38.3	-2.1

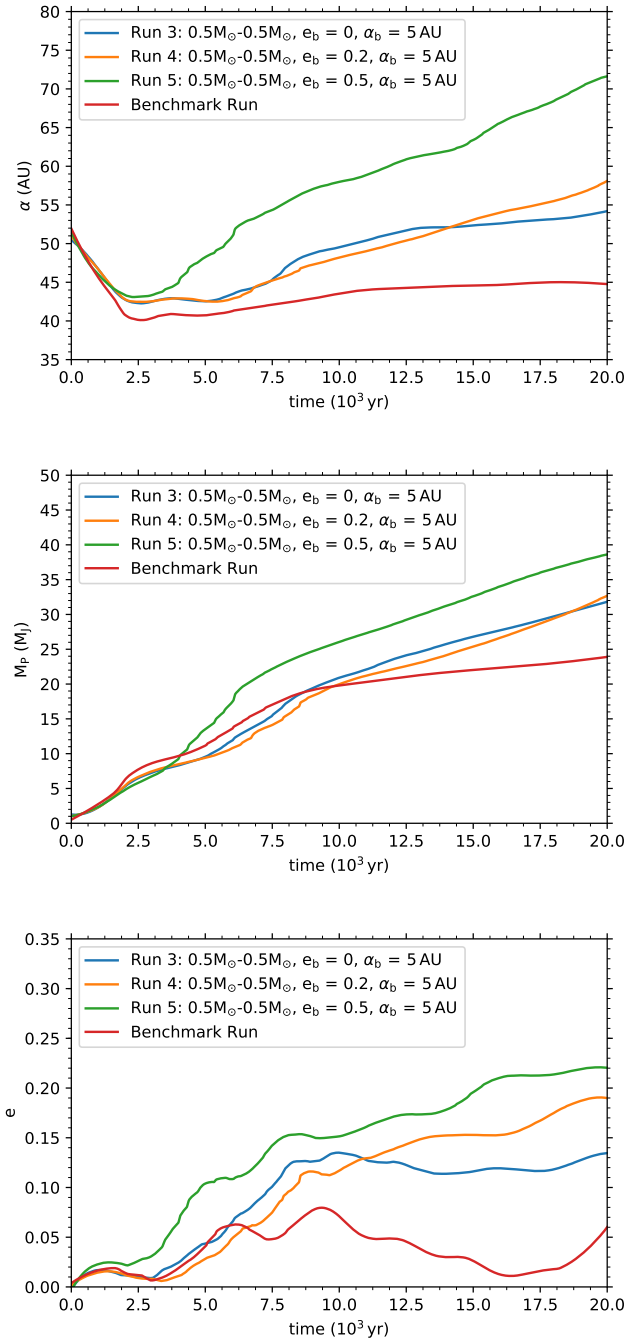

Figure 4.2: $1\,\mathrm{M_J}$ planet embedded in a disk orbiting a binary system consisting of two $0.5\,\mathrm{M_\odot}$ stars, with initial semi-major axis $\alpha_\mathrm{b} = 5\,\mathrm{AU}$ and eccentricity $e_\mathrm{b} = 0$, $e_\mathrm{b} = 0.2$ and $e_\mathrm{b} = 0.5$. (a) The evolution of the semi-major axis of the planet, (b) the evolution of the planet's mass, and (c) the evolution of the planet's eccentricity. The disk modelled here has been settled for $3\,\mathrm{kyr}$.

4.6 Run 6: 0.8 - 0.2 $M_\odot$, $\alpha_b = 1$ AU, $e_b = 0$

Fig 4.3 shows the evolution of the planet's, mass and eccentricity over a period of 20 kyr. As seen in Fig 4.3a, the planet undergoes Type I migration reaching a semi-major axis of 39 AU, which is 2% lower than the benchmark run. Once a gap in the disk begins to form at t = 2 kyr, the migration changes to a non-standard Type II outward migration. As a result of the non-standard Type II migration, the planet's semi-major axis reaches 46 AU which is 2% higher than the benchmark run. The planet's mass (see Fig 4.3b) reaches a value of $M_P = 28\,M_J$ which is 16% higher than the benchmark run. The planet's eccentricity (see Fig 4.3c) shows a significant increase compared to the benchmark run, reaching a final eccentricity of 0.21.

Table 4.7 shows a significant difference in the migration timescale. As before, the migration velocity shows differences in both magnitude and direction of migration to the benchmark run. However, it is interesting to note that despite these differences, the semi-major axis for each time does not change much.

Table 4.7: The semi-major axis α, migration timescale τ_{mig}, mass M_P and migration velocity v_{mig} of the planet at different times, for Run 6. This system consists of a $0.8\,M_\odot$ star and a $0.2\,M_\odot$ star, and initially has eccentricity $e_b = 0$ and semi-major axis $\alpha_b = 1$ AU. Here, the negative values in v_{mig} indicate the planet is migrating in an outward direction.

t (kyr)	α (AU)	τ_{mig} (kyr)	M_P (M_J)	v_{mig} (AU/kyr)
0.7	48.5	11.9	1.9	4.2
1.5	44.2	10.7	4.0	4.2
2.5	39.0	-37.7	8.8	-1.0
5	40.5	-20.3	12.3	-2.0
18	44.4	-46.5	26.8	-1.0

4.7 Run 7: 0.8 - 0.2 $M_\odot$, $\alpha_b = 1$ AU, $e_b = 0.2$

Fig 4.3 shows the evolution of the planet's semi-major axis, mass and eccentricity over a period of 20 kyr. As seen in Fig 4.3a, the planet undergoes Type I migration reaching a semi-major axis of 42 AU, a 6% increase on the benchmark run. Once a gap in the disk begins to form at t = 2 kyr, the migration changes to a non-standard Type II outward migration. As a result of the non-standard Type II migration, the planet's semi-major axis reaches 50 AU, an 11% difference to the benchmark run. The planet's mass (see Fig 4.3b) reaches a value of $M_P = 25\,M_J$, an increase of 6% on the benchmark run's value. The planet's eccentricity (see Fig 4.3c) shows an increase compared to the benchmark run, reaching a final eccentricity of 0.10.

Table 4.8 follows similar trends to that of the benchmark run, with comparable values in semi-major axis, mass and migration velocity. However, the migration timescale is considerably different at the final stages of evolution. This value is notably larger than that of the planet in the benchmark run, but also than in previous runs.

Table 4.8: The semi-major axis α, migration timescale τ_{mig}, mass M_P and migration velocity v_{mig} of the planet at different times, for Run 7. This system consists of a 0.8 $M_\odot$ star and a 0.2 $M_\odot$ star, and initially has eccentricity $e_b = 0.2$ and semi-major axis $\alpha_b = 1$ AU. Here, the negative values in v_{mig} indicate the planet is migrating in an outward direction.

t (kyr)	α (AU)	τ_{mig} (kyr)	M_P (M_J)	v_{mig} (AU/kyr)
0.7	48.5	13.2	1.9	3.7
1.5	45.2	11.1	3.7	4.2
2.5	42.6	-18.7	7.0	-2.3
5	43.2	-116.1	10.5	-0.4
18	50.1	-3255.5	25.4	-0.02

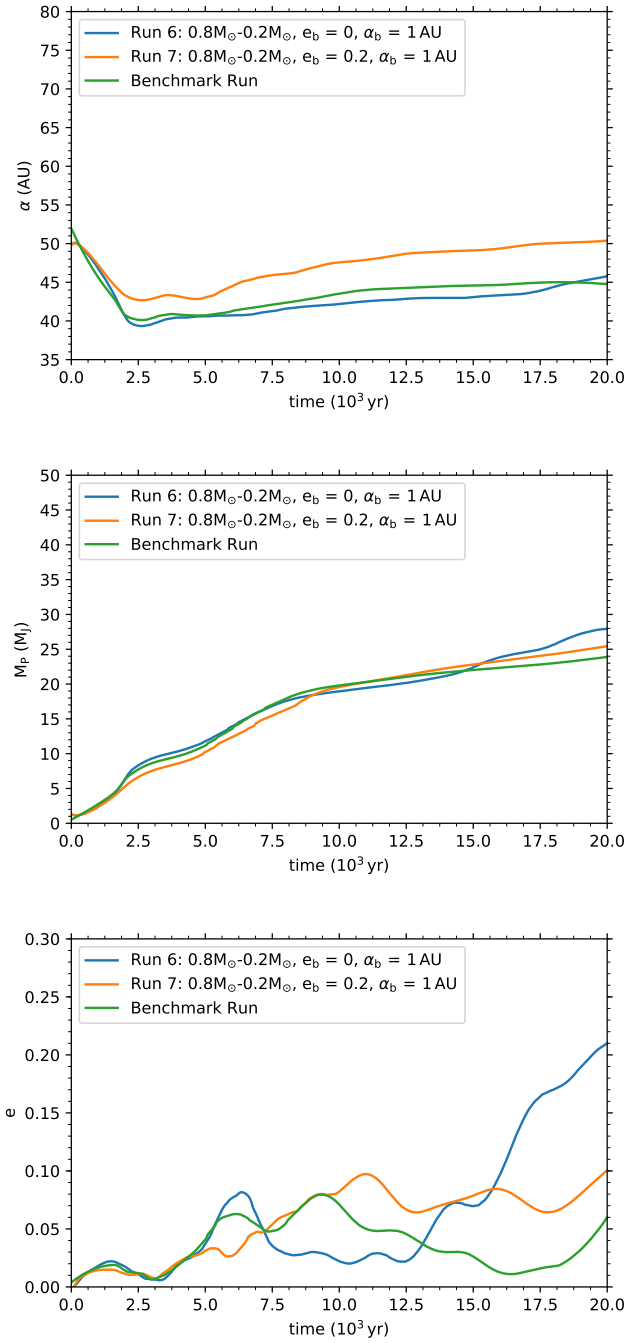

Figure 4.3: $1\,\mathrm{M_J}$ planet embedded in a disk orbiting a binary system consisting of a $0.8\,\mathrm{M_\odot}$ star and a $0.2\,\mathrm{M_\odot}$ star, with initial semi-major axis $\alpha_\mathrm{b} = 1\,\mathrm{AU}$ and eccentricity $e_\mathrm{b} = 0$ and $e_\mathrm{b} = 0.2$. (a) The evolution of the semi-major axis of the planet, (b) the evolution of the planet's mass, and (c) the evolution of the planet's eccentricity. The disk modelled here has been settled for $3\,\mathrm{kyr}$.

4.8 Run 8: 0.8 - 0.2 $M_\odot$, $\alpha_b = 5$ AU, $e_b = 0$

Fig 4.4 shows the evolution of the planet's, mass and eccentricity over a period of 20 kyr. As seen in Fig 4.4a, the planet undergoes Type I migration reaching a semi-major axis of 41 AU, a difference of 4% from the benchmark run. Once a gap in the disk begins to form at t = 3 kyr, the migration changes to a non-standard Type II outward migration. As a result of the non-standard Type II migration, the planet's semi-major axis reaches 50 AU which is 11% higher than the benchmark run. The planet's mass (see Fig 4.4b) reaches a value of $M_P = 26\,M_J$, a difference of 9% to the benchmark run. The planet's eccentricity (see Fig 4.3c) shows a increase compared to the benchmark run, reaching a final eccentricity of 0.12.

Table 4.9 is very similar to that of the benchmark run, showing similar trends and values with no significant differences.

Table 4.9: The semi-major axis α, migration timescale τ_{mig}, mass M_P and migration velocity v_{mig} of the planet at different times, for Run 8. This system consists of a $0.8\,M_\odot$ star and a $0.2\,M_\odot$ star, and initially has eccentricity $e_b = 0$ and semi-major axis α_b =5 AU. Here, the negative values in v_{mig} indicate the planet is migrating in an outward direction.

t (kyr)	α (AU)	τ_{mig} (kyr)	M_P (M_J)	v_{mig} (AU/kyr)
0.7	48.4	11.4	1.9	4.3
1.5	44.7	11.6	3.8	3.9
2.5	41.8	-17.6	7.3	-2.3
5	42.5	524.4	10.8	0.1
18	50.0	-200.0	26.1	-0.2

4.9 Run 9: 0.8 - 0.2 $M_\odot$, $\alpha_b = 5$ AU, $e_b = 0.2$

Fig 4.4 shows the evolution of the planet's, mass and eccentricity over a period of 20 kyr. As seen in Fig 4.4a, the planet undergoes Type I migration reaching a semi-major axis of 41 AU (a difference of 4% to the benchmark run). Once a gap in the disk begins to form at t = 2 kyr, the migration changes to a non-standard Type II outward migration. As a result of the non-standard Type II migration, the planet's semi-major axis reaches 50 AU (a difference of 12% to the benchmark run). The planet's mass (see Fig 4.4b) reaches a value of $M_P = 26\,M_J$, an increase of 8% on the benchmark run. The planet's eccentricity (see Fig 4.3c) shows a similar trend with a small increase compared to the benchmark run, reaching a final eccentricity of 0.08.

Table 4.10 shows no significant difference to that of the benchmark run, and the properties of the planet show similar trends. The only somewhat significant difference occurs at 5 kyr when the planet has a shorter migration timescale.

Table 4.10: The semi-major axis α, migration timescale τ_{mig}, mass M_P and migration velocity v_{mig} of the planet at different times, for Run 9. This system consists of a 0.8 $M_\odot$ star and a 0.2 $M_\odot$ star, and initially has eccentricity $e_b = 0.2$ and semi-major axis α_b =5 AU. Here, the negative values in v_{mig} indicate the planet is migrating in an outward direction.

t (kyr)	α (AU)	τ_{mig} (kyr)	M_P (M_J)	v_{mig} (AU/kyr)
0.7	48.4	11.6	1.9	4.2
1.5	44.5	10.3	3.9	4.4
2.5	41.6	-16.6	7.7	-2.5
5	41.9	50.5	11.5	0.8
18	50.0	-460.3	26.1	-0.1

4.10 Run 10: 0.8 - 0.2 $M_\odot$, $\alpha_b = 5$ AU, $e_b = 0.5$

Fig 4.4 shows the evolution of the planet's, mass and eccentricity over a period of 20 kyr. As seen in Fig 4.4a, the planet undergoes Type I migration reaching a semi-major axis of 42 AU, a difference of 2 AU or a 5% increase from the benchmark run. Once a gap in the disk begins to form at t = 2 kyr, the migration changes to a non-standard Type II outward migration. As a result of the non-standard Type II migration, the planet's semi-major axis reaches 61 AU which is 16 AU higher than the benchmark run, a significant 30% increase. The planet's mass (see Fig 4.4b) reaches a value of $M_P = 35\,M_J$, a 37% increase on the final value in the benchmark run. The planet's eccentricity (see Fig 4.3c) shows a significant increase compared to the benchmark run, reaching a final eccentricity of 0.19.

Table 4.11 shows a shorter migration timescale values when compared to the benchmark run. Other than this, the values are similar to the ones of the benchmark run.

Table 4.11: The semi-major axis α, migration timescale τ_{mig}, mass M_P and migration velocity v_{mig} of the planet at different times, for Run 10. This system consists of a 0.8 $M_\odot$ star and a 0.2 $M_\odot$ star, and initially has eccentricity $e_b = 0.5$ and semi-major axis α_b =5 AU. Here, the negative values in v_{mig} indicate the planet is migrating in an outward direction.

t (kyr)	α (AU)	τ_{mig} (kyr)	M_P (M_J)	v_{mig} (AU/kyr)
0.7	48.4	11.4	1.9	4.3
1.5	44.4	13.5	3.9	3.3
2.5	42.3	-19.3	6.9	-2.2
5	42.0	53.1	11.1	0.8
18	58.0	-76.9	33.4	-0.8

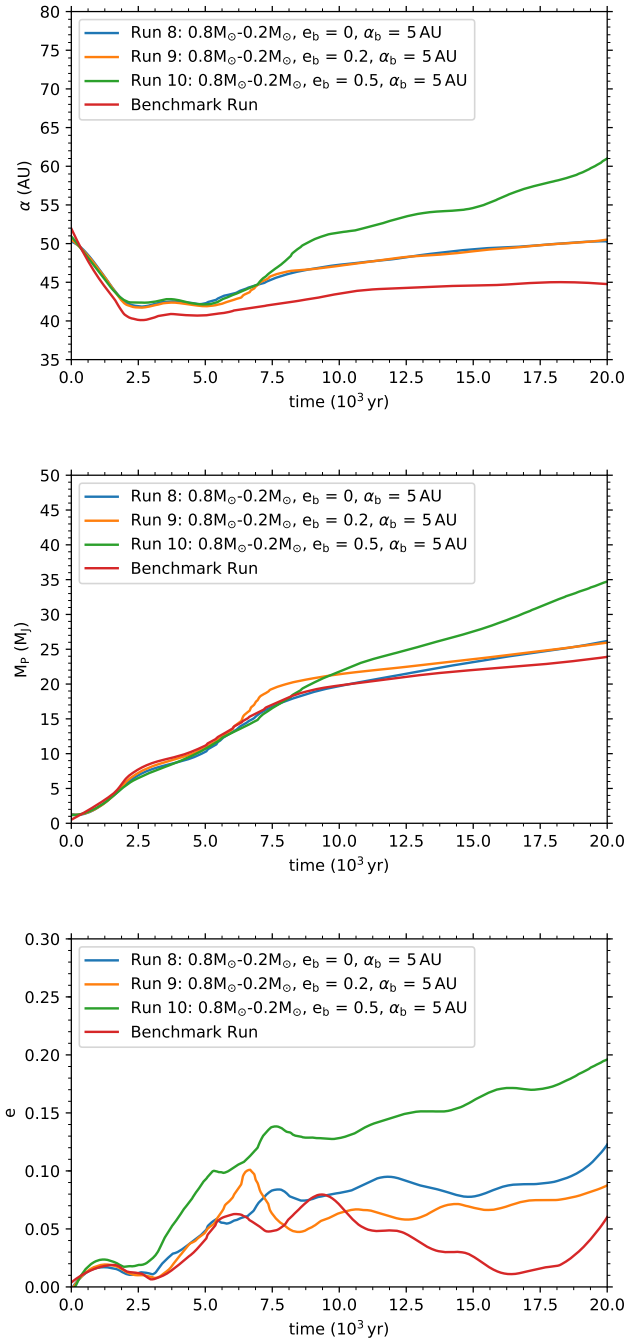

Figure 4.4: $1\,\mathrm{M_J}$ planet embedded in a disk orbiting a binary system consisting of a $0.8\,\mathrm{M_\odot}$ star and a $0.2\,\mathrm{M_\odot}$ star, with initial semi-major axis $\alpha_\mathrm{b} = 5\,\mathrm{AU}$ and eccentricity $e_\mathrm{b} = 0$, $e_\mathrm{b} = 0.2$ and $e_\mathrm{b} = 0.5$. (a) The evolution of the semi-major axis of the planet, and (b) the evolution of the planet's mass. The disk modelled here has been settled for 3 kyr.

Chapter 5

Discussion

The binary star simulations presented in the previous chapter are discussed here in the context of comparisons between the varying binary parameters.

5.1 Role of the initial binary mass ratio on the migration of the planet

The simulations with stellar initial masses 0.8 - 0.2 $M_\odot$ and 0.5 - 0.5 $M_\odot$ show similar trends with regards to the evolution of the semi-major axis of the planet (see Fig 5.2a and Fig 5.1a), i.e. a fast inward migration followed by a slow outward migration when the planet opens up a gap in the disk. However, we see that the simulations with initial stellar masses 0.5 - 0.5 $M_\odot$ result in a faster outward migration and larger final values for the semi-major axis compared to simulations with initial stellar masses 0.8 - 0.2 $M_\odot$. In a similar fashion to the semi-major axis, the mass of the planet (see Fig 5.1b and Fig 5.2b) can be seen to follow a similar trend regardless of the initial binary mass ratio of the run. We find that the simulations with initial stellar masses 0.5 - 0.5 $M_\odot$ do not result in higher final planet masses when compared with initial stellar masses 0.8 - 0.2 $M_\odot$. It can be seen that the planet is able to evolve to a

mass beyond $M_{\rm P} = 13\,{\rm M_J}$ and so can be considered a brown dwarf (Spiegel, Burrows & Milsom, 2011). This trend does not continue for the eccentricity of the planet (see Fig 5.1c and Fig 5.2c) as we see that simulations with initial stellar masses 0.5 - $0.5\,{\rm M_\odot}$ result in higher final eccentricities when compared with simulations with initial stellar masses 0.8 - $0.2\,{\rm M_\odot}$.

5.2 Role of the initial binary separation on the migration of the planet

The simulations with initial binary separation of $\alpha_{\rm b} = 1\,{\rm AU}$ follow a similar trend, reaching a final semi-major axis between $\alpha_{\rm P} = 45\,{\rm AU}$ and $\alpha_{\rm P} = 50\,{\rm AU}$ (see Fig 5.2a and Fig 5.1a). The larger initial binary separation of $\alpha_{\rm b} = 5\,{\rm AU}$ leads to a much larger range of final values for the semi-major axis, between $\alpha_{\rm P} = 45\,{\rm AU}$ and $\alpha_{\rm P} = 72\,{\rm AU}$. This trend continues for the mass of the planet, with a larger initial binary separation leading to a larger range in final mass. For $\alpha_{\rm b} = 1\,{\rm AU}$, this range is between $M_{\rm P} = 23\,{\rm M_J}$ and $M_{\rm P} = 28\,{\rm M_J}$ (see Fig 5.1b and Fig 5.2b). This range is much smaller for the runs with $\alpha_{\rm b} = 5\,{\rm AU}$, between $M_{\rm P} = 26\,{\rm M_J}$ and $M_{\rm P} = 39\,{\rm M_J}$. The planet is able to evolve to a mass beyond the brown dwarf lower mass limit of $13\,{\rm M_J}$. The evolution of the eccentricity of the planet follows a similar trend, with a larger range of final values for the runs with $\alpha_{\rm b} = 5\,{\rm AU}$ than those with $\alpha_{\rm b} = 1\,{\rm AU}$ (see Fig 5.1c and Fig 5.2c). Generally speaking, the larger initial binary separation leads to higher final values for the semi-major axis, mass and eccentricity of the planet.

5.3 Role of the initial binary eccentricity on the migration of the planet

It can be seen that increasing the initial eccentricity of the binary from $e_{\rm b} = 0$ to $e_{\rm b} = 0.2$ does not greatly affect the evolution of the planet's semi-major axis (see Fig 5.2a and Fig 5.1a). However, this is not the case when increasing this initial eccentricity to $e_{\rm b} = 0.5$. This change leads to an accelerated outward migration, reaching much higher final values for the semi-major axis. A similar trend can be seen in regards to the mass of the planet, an initial binary eccentricity of $e_{\rm b} = 0$ and $e_{\rm b} = 0.2$ lead to a similar planet mass evolution (see Fig 5.1b and Fig 5.2b). The initial binary eccentricity of $e_{\rm b} = 0.5$ leads to a similar trend but a larger final value. Again the planet is able to evolve beyond $M_{\rm P} = 13\,{\rm M_J}$ and so can be considered a brown dwarf. The planet's eccentricity follows a similar trend to that of the planet's mass, with an initial binary eccentricity of $e_{\rm b} = 0.2$ producing similar final planet eccentricities to that of $e_{\rm b} = 0$ (see Fig 5.1c and Fig 5.2c). On the other hand, an initial binary eccentricity of $e_{\rm b} = 0.5$ produces higher planet semi-major axis, mass and eccentricity than the other initial binary eccentricities.

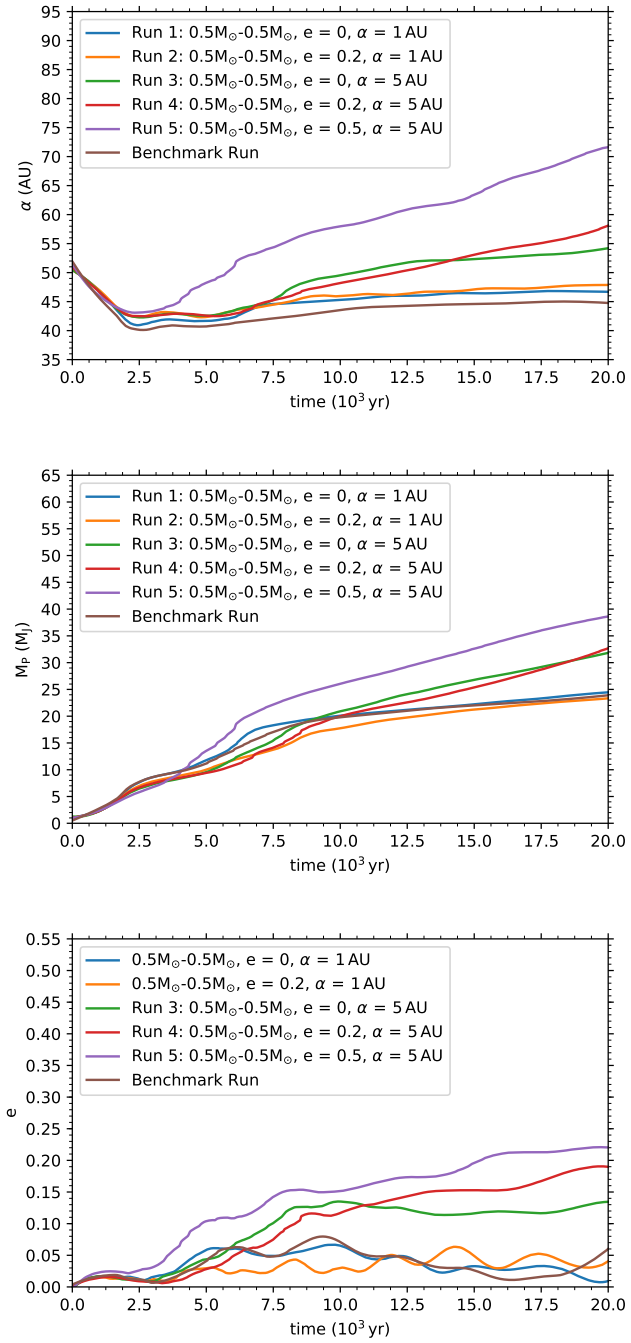

Figure 5.1: $1\,\mathrm{M_J}$ planet embedded in a disk orbiting a binary system consisting of two $0.5\,\mathrm{M_\odot}$ stars, with initial semi-major axis $\alpha_\mathrm{b} = 1\,\mathrm{AU}$ and $\alpha_\mathrm{b} = 5\,\mathrm{AU}$ and eccentricity $e_\mathrm{b} = 0$, $e_\mathrm{b} = 0.2$ and $e_\mathrm{b} = 0.5$ (as marked on the graph). (a) The evolution of the semi-major axis of the planet, (b) the evolution of the planet's mass, and (c) the evolution of the planet's eccentricity. The disk modelled here has been settled for $3\,\mathrm{kyr}$.

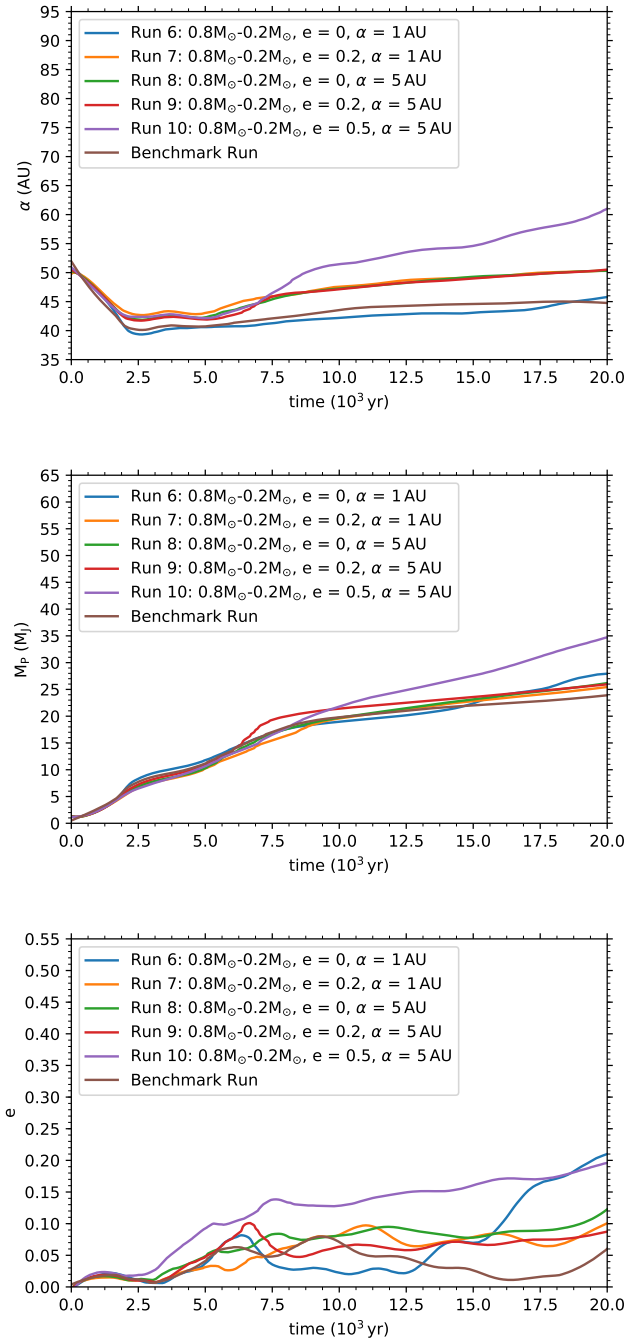

Figure 5.2: $1\,\mathrm{M_J}$ planet embedded in a disk orbiting a binary system consisting of a $0.8\,\mathrm{M_\odot}$ star and a $0.2\,\mathrm{M_\odot}$ star, with initial semi-major axis $\alpha_\mathrm{b} = 1\,\mathrm{AU}$ and $\alpha_\mathrm{b} = 5\,\mathrm{AU}$ and eccentricity $e_\mathrm{b} = 0$, $e_\mathrm{b} = 0.2$ and $e_\mathrm{b} = 0.5$. (a) The evolution of the semi-major axis of the planet, (b) the evolution of the planet's mass, and (c) the evolution of the planet's eccentricity. The disk modelled here has been settled for 3 kyr.

5.4 Caveats

The number of SPH particles used to represent the protoplanetary disk does affect the migration of a planet embedded in a disk as can be seen in Fig 3.1 once enough SPH particles have been used to reach convergence. It was noted that there was only a small difference in the migration between the benchmark simulation performed for this project and that of Stamatellos & Inutsuka (2018). We assumed that going from single to binary star simulations, the number of SPH particles used was adequate. However, it is of interest to model binary systems again with a higher number of SPH particles to see whether the simulations have indeed converged with regards to the migration of the planet. It is predicted, based on the convergence simulations, that this would have little effect on the final semi-major axis of the planet.

For the benchmark run and subsequent binary simulations, a disk relaxation period of 3 kyr was chosen. This was chosen not only because this is the duration used by Stamatellos & Inutsuka (2018) but also because it was shown that this had a relatively small effect on the migration of the planet, as seen in Fig 3.2. The final semi-major axis for the simulations using three disk relaxation times were within 2 AU of each other and so 3 kyr was chosen as an effective, and efficient duration. Relaxing the disk for a longer period of time may lead to a slower outward migration, and so it is of interest to see how this may effect the binary simulations in Chapter 4. We note however that in the benchmark run the disk was relaxed for the same duration, so as to make safe comparisons between simulations.

All of the simulations presented in this project show the planet surviving on a wide orbit but, in all cases, the planet accretes enough material from the disk to be considered a brown dwarf (i.e., above 13 M_J; Spiegel, Burrows & Milsom, 2011). One way to avoid this would be to include radiative feedback from the planet. Stamatellos (2015) compares the orbital migration of a wide orbit gas giant embedded

in a protoplanetary disk with planet radiative feedback and without. The simulation without radiative feedback shows comparable trends to that of the benchmark run, reaching a similar final semi-major axis and mass. For the simulation with irradiation from the accreting planet, the planet still survives on a relatively wide orbit ($\alpha = 15\,\mathrm{AU}$) and mass around the deuterium burning limit ($M_\mathrm{P} = 14\,\mathrm{M_J}$). This shows that including radiative feedback from the planet does effect the evolution of the planet embedded in a gaseous disk.

The binary will have an effect on the disk before the planet is embedded. Simulations with a greater initial binary separation open a wider inner cavity in the disk (around the binary). This affects the disk density profile which has the potential to affect the migration of the planet. This cavity is around 2 - 3 times the initial binary separation (Artymowicz & Lubow, 1994). However, the planet is much farther out in the disk (initially 50 AU), therefore its evolution shouldn't be affected by a significant degree.

5.5 Summary and conclusion

We used the 3D SPH code SEREN to study the migration of a planet in a circumbinary disk. We first created a benchmark run using parameters from Stamatellos & Inutsuka (2018), representing the disk with 5×10^5 SPH particles instead of 10×10^5 SPH particles; the results of this can be seen in Chapter 3. Then several binary simulations were run with the same planet/disk parameters as the benchmark run, but with extra parameters due to the presence of a second star. These parameters were varied to see their effect on the evolution of the planet embedded within the circumbinary disk. The aim of this project was to show that a planet formed through gravitational instability (GI) could survive on a wide orbit and not migrate inwards. This is to account for the observed locations of wide orbit gas giant planets. We have shown that the planet can survive in a massive circumbinary disk without

migrating inwards.

Fig 5.3 shows how the semi-major axis, the mass, the migration timescale and the migration velocity of the planet evolves with time. It can be seen (see Fig 5.3a) that the planet initially migrates inwards rapidly before migrating outwards (once the planet opens up a gap in the disk) on a much longer timescale in all runs. The planet initially undergoes Type I migration due to the rapid migration timescale of the planet and lack of a gap within the disk. The planet then undergoes a non-standard Type II migration on a longer timescale because it is able to open up a gap within the disk. The migration timescale (see Fig 5.3b) increases considerably over the course of the simulation. In all simulations, the mass of the planet (see Fig 5.3c) is able to evolve to beyond a mass of $M_{\rm P} = 13\,{\rm M_J}$. This is above the mass limit where sustained deuterium burning may occur in its interior (Spiegel, Burrows & Milsom, 2011), and the object is considered to be a brown dwarf. The migration velocity (see Fig 5.3d) for all the binary simulations follow a similar trend and show a gradual decrease as the system evolves.

The initial binary eccentricity has the greatest effect on the planet migration and therefore the final semi-major axis of the planet: higher binary eccentricity leads to faster migration and larger final semi-major axis for the planet. Furthermore we found that a smaller initial binary separation, of $\alpha_{\rm b} = 1\,{\rm AU}$, leads to a final semi-major axis between ~ 45 - $50\,{\rm AU}$. A larger initial binary separation, $\alpha_{\rm b} = 5\,{\rm AU}$, leads to values between ~ 45 - $70\,{\rm AU}$. This shows that with a larger initial binary separation, the planet migrates faster and attains a larger final semi-major axis. The initial mass ratio of the stars within the binary system can be seen to have little effect on the evolution of the planet, on the condition that the total mass of the binary is kept at $1\,{\rm M_\odot}$ as seen in Fig 5.1 and Fig 5.2.

This project studied a specific set of variables for the binary, disk and planet. Extending this work to look at variables such as different total stellar mass, extended

binary parameters and different types of exoplanet (i.e. terrestrial, hot Jupiters, etc) would be useful in gaining a deeper understanding as to how planets evolve in binary systems. Other factors to look at could involve using different disk masses to see how this would effect the migration of the planet.

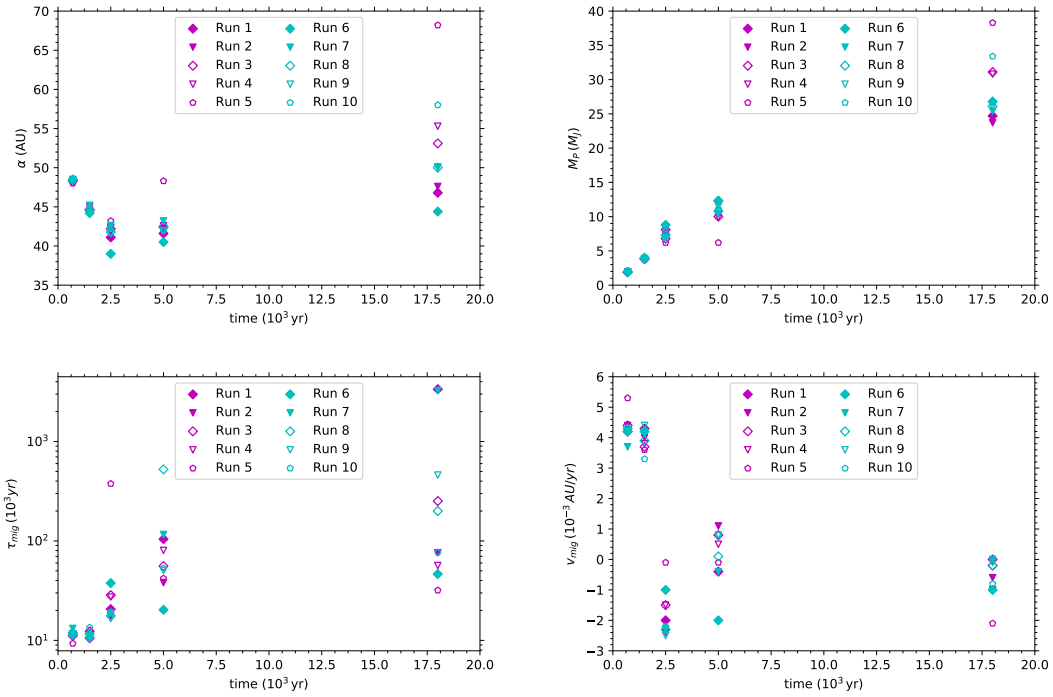

Figure 5.3: The evolution of the semi-major axis of the planet (top left), its mass (top right), its migration timescale (bottom left) and its migration velocity (bottom right) at different times for all simulations presented in this thesis. The two colours correspond to different stellar mass ratios: magenta indicates a $0.5\,M_\odot$ - $0.5\,M_\odot$ binary and cyan, a $0.8\,M_\odot$ - $0.2\,M_\odot$ binary. The three symbols indicate the initial eccentricity of the binary, with a diamond corresponding to $e_b = 0$, a triangle to $e_b = 0.2$ and a pentagon to $e_b = 0.5$. Finally filled symbols correspond to an initial binary separation of $\alpha_b = 1\,AU$ and unfilled symbols an initial separation of $\alpha_b = 5\,AU$.

Bibliography

Andrews S. M. et al., 2018, ApJL 869, L41

Armitage P. J., 2015, arXiv e-prints, arXiv:1509.06382

Armitage P. J., 2020, Astrophysics of Planet Formation, 2nd edn. Cambridge University Press, Cambridge

Artymowicz P., Lubow S. H., 1994, ApJ 421, 651

Baruteau C., Meru F., Paardekooper S.-J., 2011, MNRAS 416, 1971

Bate M. R., Bonnell I. A., Price N. M., 1995, MNRAS 277, 362

Binzel R. P., 2006, Minor Planet Bulletin, 33, 106

Bodenheimer P., Pollack J. B., 1986, Icarus 67, 391

Clarke C. J., Lodato G., 2009, MNRAS 398, L6

Dawson R. I., Johnson J. A., 2018, ARA&A 56, 175

Doyle L. R. et al., 2011, Science, 333, 1602

Dvorak R., Froeschle C., Froeschle C., 1986, in Bulletin of the American Astronomical Society, Vol. 18, p. 842

Forgan D. H., Hall C., Meru F., Rice W. K. M., 2018, MNRAS 474, 5036

Gammie C. F., 2001, ApJ 553, 174

Gingold R. A., Monaghan J. J., 1977, MNRAS 181, 375

Goldreich P., Tremaine S., 1980, ApJ 241, 425

Hallam P. D., Paardekooper S. J., 2020, MNRAS 491, 5759

Hubber D. A., Batty C. P., McLeod A., Whitworth A. P., 2011, A&A 529, A27

Ikoma M., Nakazawa K., Emori H., 2000, ApJ 537, 1013

Keppler M. et al., 2018, A&A 617, A44

Kratter K. M., Murray-Clay R. A., Youdin A. N., 2010, ApJ 710, 1375

Lin D. N. C., Pringle J. E., 1990, ApJ 358, 515

Lin M.-K., Papaloizou J. C. B., 2012, MNRAS 421, 780

Lines S., Leinhardt Z. M., Baruteau C., Paardekooper S. J., Carter P. J., 2016, A&A 590, A62

Lucy L. B., 1977, AJ 82, 1013

Matzner C. D., Levin Y., 2005, ApJ 628, 817

Mercer A., Stamatellos D., Dunhill A., 2018, MNRAS 478, 3478

Monaghan J. J., 1992, ARA&A 30, 543

Paardekooper S.-J., Dong R., Duffell P., Fung J., Masset F. S., Ogilvie G., Tanaka H., 2022, in Protostars ad Planets VII conference proceedings, eds. Shu-ichiro Inutsuka, Yuri Aikawa, Takayuki Muto, Kengo Tomida, and Motohide Tamura

Papaloizou J. C. B., Larwood J. D., 2000, MNRAS 315, 823

Pinte C. et al., 2018, ApJL 860, L13

Raghavan D. et al., 2010, ApJS 190, 1

Shakura N. I., Sunyaev R. A., 1973, A&A 24, 337

Spiegel D. S., Burrows A., Milsom J. A., 2011, ApJ 727, 57

Stamatellos D., 2015, ApJL 810, L11

Stamatellos D., Inutsuka S.-i., 2018, MNRAS 477, 3110

Stamatellos D., Whitworth A. P., Bisbas T., Goodwin S., 2007a, A&A 475, 37

—, 2007b, A&A 475, 37

Su X.-N., Xie J.-W., Zhou J.-L., Thebault P., 2021, AJ 162, 272

Tanaka H., Takeuchi T., Ward W. R., 2002a, ApJ 565, 1257

—, 2002b, ApJ 565, 1257

Teague R., Bae J., Bergin E. A., 2019, Nature 574, 378

Toomre A., 1964, ApJ 139, 1217

Wagner K., Apai D., Kratter K. M., 2019, ApJ 877, 46

Ward W. R., 1997, Icarus 126, 261

Wolszczan A., Frail D. A., 1992, Nature 355, 145